






Membership Analysis and 3D Kinematics of the Star-forming Complex around Trumpler 37 Using Gaia-DR3

Swagat R. Das^{1,2} , Saumya Gupta², Prem Prakash³, Manash Samal⁴ , and Jessy Jose² ¹ Departamento de Astronomía, Universidad de Chile, Las Condes, 7591245 Santiago, Chile; swagat@das.uchile.cl, dasswagat77@gmail.com² Indian Institute of Science Education and Research (IISER) Tirupati, Rami Reddy Nagar, Karakambadi Road, Mangalam (P.O.), Tirupati 517507, India³ Department of Physics, Indian Institute of Technology (IIT) Hyderabad, India⁴ Physical Research Laboratory, Ahmedabad, Gujarat, India

Received 2022 December 28; revised 2023 February 2; accepted 2023 February 7; published 2023 April 27

Abstract

Identifying and characterizing young populations of star-forming regions are crucial to unraveling their properties. In this regard, Gaia-DR3 data and machine-learning tools are very useful for studying large star-forming complexes. In this work, we analyze the ~ 7.1 deg² area of one of our Galaxy's dominant feedback-driven star-forming complexes, i.e., the region around Trumpler 37. Using the Gaussian mixture and random-forest classifier methods, we identify 1243 highly probable members in the complex, of which $\sim 60\%$ are new members and are complete down to the mass limit of $\sim 0.1\text{--}0.2 M_{\odot}$. The spatial distribution of the stars reveals multiple clusters toward the complex, where the central cluster around the massive star HD 206267 reveals two subclusters. Of the 1243 stars, 152 have radial velocity, with a mean value of -16.41 ± 0.72 km s⁻¹. We investigate stars' internal and relative movement within the central cluster. The kinematic analysis shows that the cluster's expansion is relatively slow compared to the whole complex. This slow expansion is possibly due to newly formed young stars within the cluster. We discuss these results in the context of hierarchical collapse and feedback-induced collapse mode of star formation in the complex.

Unified Astronomy Thesaurus concepts: [Star formation \(1569\)](#); [Open star clusters \(1160\)](#); [Star forming regions \(1565\)](#)

Supporting material: machine-readable tables

1. Introduction

Star formation is one of the most complicated yet least understood phenomena in the field of astrophysics. Most of the stars form in clusters (Blaauw 1964; Elmegreen 1983; Lada 1987; Clarke et al. 2000; Megeath et al. 2004; Bonnell et al. 2008; Portegies Zwart et al. 2010; Gieles & Portegies Zwart 2011; Bastian et al. 2012) by the fragmentation and hierarchical collapsing of molecular clouds (Larson 1981; Elmegreen & Scalo 2004; Mac Low & Klessen 2004; McKee & Ostriker 2007). Star clusters are unique tracers of galactic properties such as their origin, dynamics, and evolution (Kroupa 2008; Ferraro et al. 2016). In addition to this, such studies aid in investigating the kinematics, dispersion, and evolution of the star-forming environment (Karnath et al. 2019; Kuhn et al. 2019; Pang et al. 2020). Clusters with massive O- and B-type stars serve as important laboratories for star formation since these massive stars ionize their surroundings, create H II regions, and shape the evolution of the low-mass star population in the vicinity through their feedback effects (Samal et al. 2014; Jose et al. 2016; Das et al. 2017, 2021; Zavagno et al. 2020; Gupta et al. 2021; Pandey et al. 2022). Hence, the identification and characterization of cluster members are essential to investigate various star formation properties, such as stars formed hierarchically by the natural collapse of clumpy molecular clouds or by the collapsing gas formed through sweeping and compression of the cold neutral

gas by the H II regions and bubbles. The distinction between these processes is important in understanding the net outcome of star formation, such as star formation efficiency (SFE) and star formation rate (SFR) due to various modes of star formation processes (Dale et al. 2012, 2013; Walch et al. 2015).

The Global Astrometric Interferometer for Astrophysics (Gaia; Gaia Collaboration et al. 2016) data have revolutionized the identification and investigation of the various scientific properties of Galactic clusters (Koposov et al. 2017; Gaia Collaboration et al. 2018c; Bossini et al. 2019; Kuhn et al. 2019; Damian et al. 2021). The Gaia-DR2 (Gaia Collaboration et al. 2018b) data contain five parameters (positions, parallax, and proper motions) and astrometric solutions of ~ 1.3 billion of stars up to the *G*-band magnitude of 21 (Gaia Collaboration et al. 2018b). Compared to Gaia-DR2, Gaia-EDR3 improved the accuracy in proper-motion and parallax measurements by factors of 2 and 2.5, respectively (Gaia Collaboration et al. 2021). This accuracy improvement has benefited the better distinction of cluster members, especially for distant clusters. The final data release, Gaia-DR3, has significantly improved the radial-velocity measurement of stars. Gaia-DR3 preserves the astrometry properties of Gaia-EDR3 but has improved the radial-velocity measurement compared to Gaia-DR2 in terms of accuracy and number of stars. This work aims to identify the new member population associated with the star-forming complex around Trumpler 37 (Tr 37) in IC 1396 using the multidimensional Gaia-DR3 data and machine-learning techniques.

This work is arranged as follows. We describe the complex IC 1396 in Section 2. In Section 3, we present the analysis and results of this work. This includes the details of Gaia-DR3 data,



Original content from this work may be used under the terms of the [Creative Commons Attribution 4.0 licence](#). Any further distribution of this work must maintain attribution to the author(s) and the title of the work, journal citation and DOI.

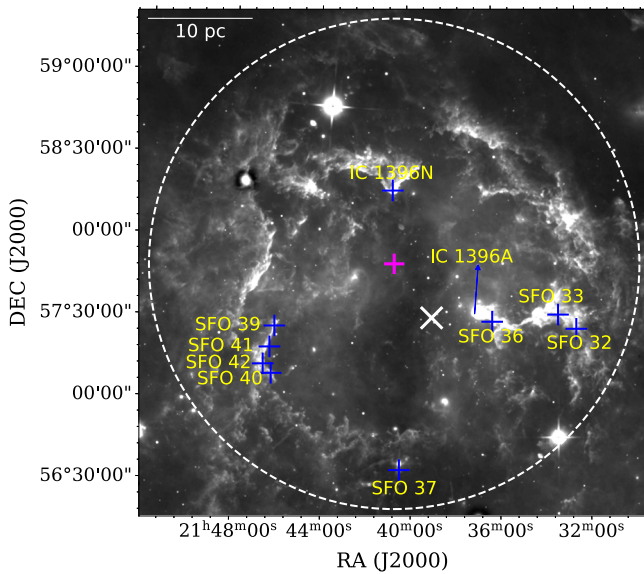


Figure 1. This figure shows the WISE $22\ \mu\text{m}$ image of the IC 1396. The cross (“ \times ”) shows the position of the massive star HD 206267. The major globules from Sugitani et al. (1991) are marked by “+” symbols, and their IDs are mentioned. The white dashed circle (radius of 1.5°) is the region considered in this study for searching members using the Gaia-DR3 data. The center of the circle ($\alpha = 21:40:39.28$ and $\delta = +57:49:15.51$) is marked by a magenta “+.” A scale bar of 10 pc is shown in the top-left corner.

the membership analysis using the machine-learning approach, and the properties of the identified members. In Section 4, we discuss the various physical properties of IC 1396 derived using new members identified in this work along with literature-based members. We discuss the complex’s 3D kinematic property and star formation history in Section 5. We summarize our work in Section 6.

2. IC 1396

The star-forming complex around Trumpler 37 (Tr 37; Trumpler 1930) in IC 1396, shown in Figure 1, is one of the classic examples of H II regions with a simple circular morphology and which is part of the Cepheus OB2 complex (de Zeeuw et al. 1999). IC 1396 has relatively low ($A_V < 5$ mag) foreground reddening (Sicilia-Aguilar et al. 2005; Getman et al. 2012; Nakano et al. 2012). The star-forming complex is believed to be powered by the massive star (HD 206267) of spectral type O6 V, located near the center (Stickland 1995). This H II region is well known for its association with more than 20 bright-rimmed clouds (BRCs; Sugitani et al. 1991), fingertip structures, and elephant trunk structures in and around them, suggesting feedback effect from the massive central star (Schwartz et al. 1991; Froebrich et al. 2005; Saurin et al. 2012). The well-known BRCs at the peripheries of the H II region (IC 1396A and IC 1396N) have often been referred to as the best examples of feedback-driven star formation (Sicilia-Aguilar et al. 2004, 2006a; Getman et al. 2007; Choudhury et al. 2010; Sicilia-Aguilar et al. 2013; Panwar et al. 2014; Sicilia-Aguilar et al. 2014, 2019), with many previous studies focused around IC 1396A. Using Gaia-DR2 data of the previously identified members, Sicilia-Aguilar et al. (2019) estimate a distance of 945^{+90}_{-73} pc, which is consistent within errors with the previous estimate of Contreras et al. (2002). Also, Sicilia-Aguilar et al. (2005) obtained a mean age of $\sim 2\text{--}4$ Myr of the complex based on the spectroscopically

identified members. The modest distance and low foreground reddening make IC 1396 an ideal target for understanding the evolution of the H II region and exploring the low-mass population associated with the complex.

We present the entire field of view of IC 1396 using the WISE $22\ \mu\text{m}$ image in Figure 1. The region exhibits a prominent mid-infrared cavity of radius $\sim 1.5^\circ$, which signifies the role of UV photons from the associated massive stars toward the gas and dust content of the cluster. BRCs, fingertip, and elephant trunk structures are visible toward the periphery of the H II region displaying the feedback-driven activity in the region. To better understand the evolution of the host H II region and its possible impact on the next-generation stars associated with BRCs/globules and hence the star formation history of the complex, it is important to identify the total member population of the whole complex. There have been many studies in the past in search of the young stellar objects (YSOs) associated with the complex, however these surveys have different area coverage and sensitivity. A brief detail of the membership analysis from previous works toward the complex is given in the next subsection.

Gaia-DR3, due to its improvement in both photometry, astrometry, and radial-velocity measurements over Gaia-DR2, is the best data set to obtain the membership population of the complex and, subsequently, its physical properties.

2.1. Member Population from Previous Studies

The identified member population toward this complex in previous studies can broadly be divided into four categories. Spectroscopically identified members (Contreras et al. 2002; Sicilia-Aguilar et al. 2006b, 2013), Spitzer-based NIR-excess sources (Reach et al. 2004; Sicilia-Aguilar et al. 2006a; Morales-Calderón et al. 2009), identification based on H_α excess emission (Barentsen et al. 2011; Nakano et al. 2012), and X-ray emission sources (Getman et al. 2007; Mercer et al. 2009; Getman et al. 2012). In addition, a relatively more recent analysis by Silverberg et al. (2021) combines the near-infrared data from UKIRT with X-ray data from XMM-Newton to identify Class III YSO cluster members in a region covering the IC 1396A region. Altogether, there are 1791 candidate members identified in the literature. Apart from this, Cantat-Gaudin et al. (2018) have analyzed a large number (1229) of Milky Way clusters using the Gaia-DR2 catalog. They used an unsupervised machine-learning technique to detect the member stars. They have listed the stars with membership probability greater than 50% as candidate cluster members. For IC 1396, they have identified 460 stars within a radius of 0.7° centered at $\alpha = 21:38:58.80$ and $\delta = +57:30:50.40$. This region mostly covers the central part of the complex around the massive star HD 206267. Recently, Pelayo-Baldarrago et al. (2023),⁵ using Gaia-EDR3 and optical spectroscopic analysis of the complex, provided the distance, age, and distribution of the the member sources. In Table 1, we summarize details of the area covered and the number of stars retrieved in individual work.

We detect the member stars within a region of 1.5° radius, shown as a white dashed circle in Figure 1, and aim to detect new members of the complex. In Section 3.4, we compare the catalog identified in this work with the literature.

⁵ This article is in press, hence a detailed comparison of the sources could not be incorporated.

Table 1
Area Covered and the Number of Stars Obtained in Previously Published Literature

Work	No. of Stars	Radius (degree)	R.A. (J2000)	Decl. (J2000)
Contreras et al. (2002)	66	0.5	21:39:09.89	+57:30:56.07
Sicilia-Aguilar et al. (2006b)	172	0.6	21:37:54.41	+57:33:15.32
Sicilia-Aguilar et al. (2013)	67	0.25	21:37:03.17	+57:29:05.43
Reach et al. (2004)	17	0.12	21:36:33.09	+57:29:13.83
Sicilia-Aguilar et al. (2006a)	57	0.15	21:36:39.73	+57:29:28.45
Morales-Calderón et al. (2009)	69	0.15	21:36:36.32	+57:29:54.78
Barentsen et al. (2011)	158	1.5	21:40:00.43	+57:26:42.60
Nakano et al. (2012)	639	1.4	21:39:48.76	+57:30:31.56
Getman et al. (2007)	24	0.1	21:40:36.73	+58:15:37.51
Mercer et al. (2009)	39	0.15	21:38:54.67	+57:29:17.61
Getman et al. (2012)	457	0.25	21:37:05.85	+57:32:30.06
Silverberg et al. (2021)	421	0.37	21:33:59.30	+57:29:30.76
Cantat-Gaudin et al. (2018)	460	0.7	21:38:58.80	+57:30:50.40

3. Analysis and Results

3.1. Data from Gaia-DR3

To obtain the Gaia-based membership of the region, we use the Gaia-DR3 catalog, downloaded from the Gaia archive (Gaia Collaboration 2022).⁶ We retrieve all the sources within the 1.5 radius centered at $\alpha = 21:40:39.28$ and $\delta = +57:49:15.51$. The search region is shown as the white dashed circle in Figure 1, covering the entire IC 1396 complex. To identify the likely cluster members of this complex, we select sources based on the following criteria. All the selected sources must have positive parallax values ($\pi > 0$ mas). We consider all sources with proper motion ranging between $|\mu_\alpha \cos \delta| \leq 20$ mas yr⁻¹ and $|\mu_\delta| \leq 20$ mas yr⁻¹. This constraint on the proper-motion values removes a large fraction of contaminants (Gao 2018a, 2018b). All the sources we consider must have magnitude values in the *G*, *BP*, and *RP* bands. We thus obtain 458,875 sources within the 1.5 region, which satisfy all the criteria mentioned above.

Following the histogram turnover method (Winston et al. 2007; Jose et al. 2013, 2017; Getman et al. 2017; Damian et al. 2021), we obtain the 90% photometry completeness limits of the *G*, *BP*, and *RP* bands to be 20.5, 21.5, and 19.5 mag, respectively. This is in agreement with the survey completeness, which is between $G \approx 19$ and $G \approx 21$ mag (Gaia Collaboration et al. 2021). The corresponding mass-completeness limits are estimated in Section 4.2.

3.2. Membership Analysis

Detecting the membership of a star-forming region is the first step toward analyzing its various star formation properties. If the regions are large (e.g., IC 1396, Lupus) or the regions are not isolated, then the identification of members is not straightforward. Several authors have used different methods to achieve this. Here we briefly summarize the different methods of segregating the member stars from the field population. The pioneering works of Sanders (1971) and Vasilevskis et al. (1958) adopt the probability measurements of stars using their proper motions to confirm their membership. In these works, they modeled the distribution of stars in the vector point diagram (VPD) using a bivariate Gaussian mixture model (GMM). Later, adding the celestial coordinates of stars to their proper motions, Kozhurina-Platais et al. (1995) refined the membership probabilities. Some researchers selected the

stars by partitioning the data space into bins (Platais 1991; Lodiou et al. 2012). In another work, Balaguer-Núñez et al. (2007) tried to separate the cluster members from the field stars based on their probability density in their VPD space. The broadband photometry is also considered as a tool to separate the cluster members from field stars with the help of color-magnitude (CMD) and color-color diagrams (CCD) (Deacon & Hambly 2004; Balaguer-Núñez et al. 2007). Krone-Martins & Moitinho (2014) have developed a method of computing membership probabilities in an unsupervised manner from the combination of celestial coordinates and photometric measurements. Their method is unsupervised photometric membership assignment in stellar clusters (UPMASK). The method of Sarro et al. (2014) and Olivares et al. (2019) uses astrometric and photometric features of the stars for membership analysis. Then they apply the GMM with different components to model the field population and follow the Bayesian information criteria to choose a model. Then this method modeled the cluster with GMM in the astrometric space and a principal curve in the photometric space. Several recent works have used this methodology for membership analysis (Galli et al. 2020, 2021). The use of unsupervised and supervised computation of membership probabilities has also followed in several works in the recent past. In these works, the unsupervised GMM is used to generate a first catalog for the computation of supervised membership probability. These works used the random forest (RF; Breiman 2001; Pedregosa et al. 2011) classifier of the machine-learning algorithm for the supervised computation of membership probability. Recently, Muzic et al. (2022) used various CMDs effectively along with the RF classifier to obtain the membership of NGC 2244.

So both astrometry and photometric properties of stars play a crucial role in identifying member populations. As discussed, unsupervised and supervised membership probability estimation works efficiently and effectively. The crucial part of this method is preparing a training set, which comes through the unsupervised estimation, the GMM method. However, GMM suffers difficulty in filtration if the field contamination is relatively high. A safe way to overcome this difficulty is to combine the photometric properties in CMDs to obtain a set of stars, which can be used for the supervised membership probability estimation. Our present analysis uses the various CMDs to refine the member population obtained from the GMM method. We use a few CMDs and theoretical isochrones with prior knowledge about the nature of the star-forming

⁶ <https://gea.esac.esa.int/archive/>

complex from earlier studies. This helps to derive a cleaner member data set, which is used as a training set to derive the supervised membership probability using the RF classifier. We discuss the application of both GMM and RF in the following. More detail about the GMM method is given in Appendix A.

3.2.1. Applying the Gaussian Mixture Model

We use five parameters (proper motions, parallax, and positions) for our clustering analysis using GMM. We have neither used the errors of the corresponding parameters nor the magnitude and color values as input parameters since they do not follow the Gaussian distributions. The GMM method fails drastically in cluster identification if we apply it to all stars (i.e., 458,875 sources within the whole area). This is one of the significant limitations of the GMM method, which is also observed in other analyses (Gao 2018a, 2018b). The possible reasons for this failure are described by Cabrera-Cano & Alfaro (1990). They pointed out that if the ratio between field stars and member stars is very high, it might cause an issue in clustering analysis using GMM. The other possible reason could be that the field stars do not follow a Gaussian distribution.

To avoid the above issues related to the GMM method, we try to apply GMM over a small sample with minimum field-star contamination. We must remember that obtaining the member population is not straightforward when dealing with a large star-forming complex such as IC 1396, whose radius is $\sim 1.5^\circ$. The reason is that the member populations of IC 1396 might not follow a single Gaussian distribution in their proper-motion parameters, unlike an isolated cluster. So, we have to choose a small region very carefully, such that the astrometric and photometric properties of the stars in this region should represent the whole complex, and also, at the same time, the field-star contamination should be as minimal as possible. In this work, we choose a conservative small central circular region of radius $30'$ around the coordinate mentioned in Section 3.1. We also use information from previous studies to minimize regional field-star contamination. The previous studies suggest the distance of IC 1396 to be ~ 1 kpc (Contreras et al. 2002; Sicilia-Aguilar et al. 2019). So we consider the stars that lie within the distance of 700 pc and 1100 pc to run the GMM algorithm so that we can safely throw the stars that lie outside the distance range. With these conditions, there are 6263 stars within the circular region of radius $30'$. We apply GMM on the 6263 stars, and based on the unsupervised membership estimation, we try to retrieve an initial sample of member stars, which will be used for the membership analysis based on supervised probability computation using the RF method.

Since the stars can broadly be separated into two groups as cluster members and field contaminants, we apply the GMM method with two components on these 6263 stars, and we retrieve 3760 stars with $P_{\text{GMM}} \geq 0.8$, and the remaining 2503 stars are mostly nonmembers consisting of the field-star population. A few possible combinations of CMDs and the VPD of these 6263 stars (gray), along with the extracted 3760 stars (black) from GMM, are shown in Figure 2. As seen from the VPD diagram (Figure 2(a)), the 3760 stars populate the central black region. This is expected since the member stars of a region usually lie within a narrow circular distribution in the VPD plot. However, the VPD plot and distribution of the 3760 stars on the CMDs show that the member stars are still associated with contamination. There could be a few probable

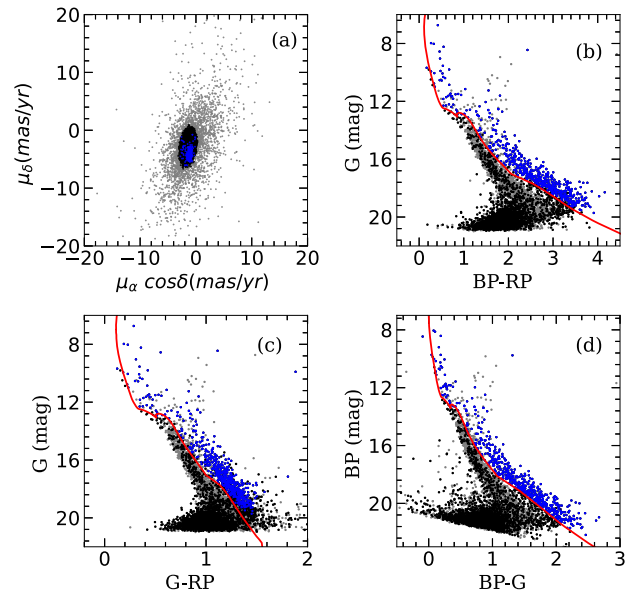


Figure 2. (a) shows the proper-motion vector point diagram (VPD), and (b), (c), and (d) show the various combination of CMDs of the 6263 sources within a $30'$ radius. On the CMDs, the red curve displays the PARSEC isochrone (Chen et al. 2014) for 10 Myr, plotted after correcting for a distance of 900 pc and extinction of $A_V = 1$ mag (discussed in Section 4.2). In all the plots, the gray dots are 6263 stars, and the black dots are the 3760 stars separated by the GMM method with a probability greater than 80%. Out of the 3760 stars, 577 stars lying to the right of 10 Myr in all the CMDs are shown in blue dots.

reasons for this. In this analysis, we do not apply any constraint on the magnitude of stars to filter a maximum number of member stars in the fainter end. However, the fainter stars have higher uncertainty and are less reliable. The other possible reason is that in the case of a giant star-forming region such as IC 1396, the member stars might have a slightly wider distribution in proper motion compared to an isolated stellar cluster. That again increases the chance of contamination in the member star population. So it requires a double check to minimize contamination from the 3760 stars extracted from the GMM method. For this, we use various CMDs, shown in Figure 2. Though the cluster associated with IC 1396 has a mean age of ~ 2 –4 Myr (Sicilia-Aguilar et al. 2005), there is a spread in age up to 10 Myr for some stars, so here we consider only those sources younger than 10 Myr as members. This further removes a significant fraction of contaminated stars from the member population. There are 577 stars left, which are more reliably member stars. These 577 stars are shown as blue dots in Figure 2. The selected member stars show a distribution that is largely indistinguishable from the field stars, likely due to the large number of field stars along the line of sight compared to the small number of cluster stars. However, compared to the distribution of field stars, the distribution of member stars peaks at different locations and shares conservative space in the VPD diagram. For a training sample for the RF method, we keep the 577 stars as member stars and the 2503 stars as nonmember stars.

3.2.2. Applying the Random-forest Classifier Method

In this section, we apply the supervised machine-learning technique RF classifier to identify the membership of the entire complex. This technique is an ensemble of machine-learning decision trees for classification and regression tasks. Due to its

robustness, the RF technique is widely used in the astrophysical field (Dubath et al. 2011; Brink et al. 2013; Liu et al. 2017; Gao 2018a, 2018b; Lin et al. 2018; Plewa 2018; Mahmudun-nobe et al. 2021). In this work, we use the Python-based RF classifier available in the scikit-learn package.⁷

Before using RF on the total population to identify member stars, we need to train the machine, as described in Appendix B. After checking RF’s efficiency, we run the RF method to obtain the most probable population of the whole complex. The relative importance of the parameters in separating the member and nonmember stars is also listed in Appendix B. After training the machine with the training set retrieved from the GMM method, we ran the RF classifier on a total of 458,875 stars located in the direction of the complex IC 1396. Out of these stars, we need to retrieve the most reliable member population of the complex. As described in Appendix B, while training the machine, a few color and magnitude terms also become essential in segregating members from nonmember populations. In order to make the detection more robust, we can use the parallax parameter to filter out the nonmember stars. Here, we run RF on the stars ($\sim 70,000$), which lie within the parallax range of 0.8 to 1.6 mas. With this, we can use the color and magnitude parameters effectively; otherwise, this could increase more unlikely sources.

RF provides a membership probability to each star based on its training in the previous step. In our analysis, we retrieve 1803 likely possible members with a probability value of $P_{\text{RF}} \geq 0.6$. Details of the 1803 likely member stars are listed in Table 2. Of these 1803 stars, 1243 have a high-probability value of $P_{\text{RF}} \geq 0.8$. Hereafter we use these highly probable candidate members for follow-up analysis. In this work, the massive star HD 206267 has $P_{\text{RF}} < 0.6$. HD 206267 is a multiple-star system of spectral type O5V–O9V and an older member of the cluster (Peter et al. 2012; Maíz Apellániz & Barbá 2020). The RUWE (renormalized unit weight error), parallax, $\mu_{\alpha} \cos \delta$, and μ_{δ} of the star are 5.07, 1.360 ± 0.218 mas, -1.951 ± 0.120 , and -5.493 ± 0.281 mas yr⁻¹, respectively. The multiple stellar systems resulted in higher RUWE values and proper motions. The radial velocity of the star is -24.8 ± 1.4 km s⁻¹ (Brandt 2021), which is well within the radial-velocity distribution of the member stars (Figure 11). This is a direct confirmation of its membership. Also, many earlier studies using multiwavelength data sets show the connection of the massive star with the star-forming complex (Patel et al. 1995; Getman et al. 2012; Sicilia-Aguilar et al. 2014, 2015, 2019). In Figure 3, we plot the proper-motion VPD plot for all 458,875 stars. The member stars with $P_{\text{RF}} \geq 0.8$ identified by RF are shown as blue dots. This plot shows that the members are concentrated within a narrow range of proper-motion values.

The G versus $G - \text{RP}$ CMD is shown in Figure 9 for the member stars ($P_{\text{RF}} \geq 0.8$) within the region of radius $1^{\circ}5$ (shown in Figure 1). All the identified member stars indicate a well-defined pre-main-sequence locus on the CM diagram. In Figure 4, we overplot the likely members on the $22 \mu\text{m}$ WISE image, highlighting their distribution as a function of their P_{RF} value. An overdensity of the source distribution is visible in the central part of IC 1396. Within the complex, the stars display a diagonal distribution ranging from the BRC IC 1396A to the IC 1396N. Most of the stars are clustered around the massive star

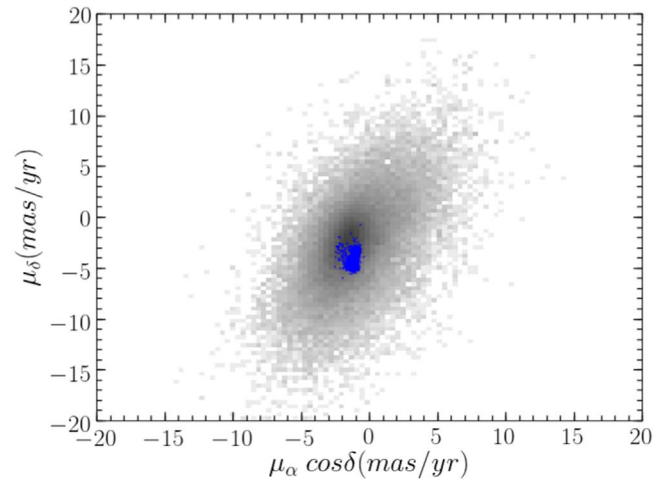


Figure 3. The VPD of all the 458,875 stars is shown as a gray density plot. The blue dots indicate the member population with $P_{\text{RF}} \geq 0.8$.

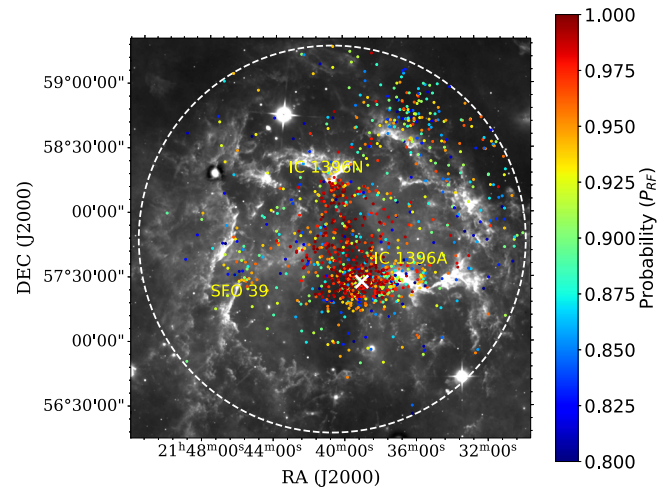


Figure 4. Spatial distribution of the likely cluster members identified from the RF method on the WISE $22 \mu\text{m}$ band. The white “x” symbol marks the position of the massive central star HD 206267. The candidate members’ color code is based on their P_{RF} values, and their color bar is also shown. Locations of the BRCs IC 1396A, IC 1396N, and SFO 39 are labeled on the plot.

HD 206267, shown as the white “x” symbol in the figure. IC 1396N is also associated with a small cluster. A tiny clustering of stars is also visible toward the tip of BRC SFO 39. A small fraction of stars is also seen to be randomly distributed all around the complex. A clustering of stars is also found toward the northern periphery of the complex. The overall distribution of stars is higher toward the west than the east of the complex.

3.3. Characteristics of the Member Stars

In Figure 5, we show histogram distributions of the RUWE,⁸ parallax, and proper motions of member stars detected in this work. Table 3 provides the range of these parameters. The RUWE parameter provides a measure of astrometric solutions. The RUWE value of around 1.0 is expected for sources where the single-star model provides a good fit for the astrometric observations. Stars with a RUWE greater than 1.4 are considered resolved doubles (Gaia Collaboration et al. 2021).

⁷ <https://scikit-learn.org/stable/modules/generated/sklearn.ensemble.RandomForestClassifier.html>

⁸ https://gea.esac.esa.int/archive/documentation/GDR2/Gaia_archive/chap_datamodel/sec_dm_main_tables/ssec_dm_ruwe.html

Table 2
List of the Gaia-based Member Population Identified Using the RF Method

Star No.	Source_ID	R.A. (2000) (degree)	Decl. (2000) (degree)	RUWE	Parallax (mas)	pmra (mas yr ⁻¹)	pmdec (mas yr ⁻¹)	<i>G</i> (mag)	BP (mag)	RP (mag)	<i>P</i> _{RF}
1	2199254363461774976	327.6486	57.3557	0.922	1.204 ± 0.178	-2.553 ± 0.232	-3.151 ± 0.194	18.80	20.60	17.56	0.716
2	2199259135157676160	327.6364	57.4715	1.055	1.299 ± 0.157	-2.162 ± 0.194	-3.075 ± 0.156	18.57	20.34	17.33	0.788
3	2202373918467694208	327.6372	58.4742	0.951	0.940 ± 0.012	-1.580 ± 0.016	-3.890 ± 0.012	12.04	13.02	11.07	0.682
4	2202263554985973760	327.4235	57.5640	0.999	1.032 ± 0.022	-3.746 ± 0.027	-4.302 ± 0.024	15.18	15.95	14.30	0.682
5	2202263898586937216	327.3769	57.5977	1.043	1.009 ± 0.013	-4.326 ± 0.016	-4.777 ± 0.014	11.15	11.53	10.57	0.664
6	2202264173461259648	327.4919	57.6289	0.964	1.018 ± 0.011	-3.333 ± 0.012	-2.184 ± 0.011	12.53	13.71	11.46	0.682
7	2202264895015605248	327.1520	57.5298	0.962	1.017 ± 0.014	-3.234 ± 0.017	-4.564 ± 0.015	14.04	14.82	13.16	0.780
8	2202267918672723968	327.2893	57.6506	0.852	1.094 ± 0.012	-2.117 ± 0.014	-4.260 ± 0.012	11.20	11.44	10.80	0.828
9	2202275267350056320	327.5741	57.8185	0.981	1.025 ± 0.069	-1.073 ± 0.076	-3.113 ± 0.082	17.59	19.09	16.42	0.702
10	2202278845069508736	327.1886	57.7081	1.014	1.049 ± 0.030	-1.048 ± 0.035	-4.333 ± 0.033	15.98	17.29	14.84	0.766

Note. The table provides the source ID, positions, parallax, proper motions, and magnitude values in the *G*, BP, and RP bands along with *P*_{RF} values of 1803 stars identified with *P*_{RF} ≥ 0.6. For analysis in this paper, we consider stars with *P*_{RF} ≥ 0.8.

(This table is available in its entirety in machine-readable form.)

Table 3
Range, Mean, Median, and Standard Deviation of the RUWE, Parallax, and Proper Motions of the 1243 Member Stars

Parameter	Range	Mean	Median	SD
RUWE	0.77 – 13.79	1.12	1.02	0.59
Parallax (mas)	0.834 ± 0.162 – 1.564 ± 0.184	1.085 ± 0.003	1.078	0.109
$\mu_\alpha \cos \delta$ (mas yr ⁻¹)	-2.506 ± 0.006 – 0.378 ± 0.015	-1.194 ± 0.002	-1.187	0.325
μ_δ (mas yr ⁻¹)	-6.011 ± 0.216 – 0.764 ± 0.014	-4.215 ± 0.004	-4.404	0.712

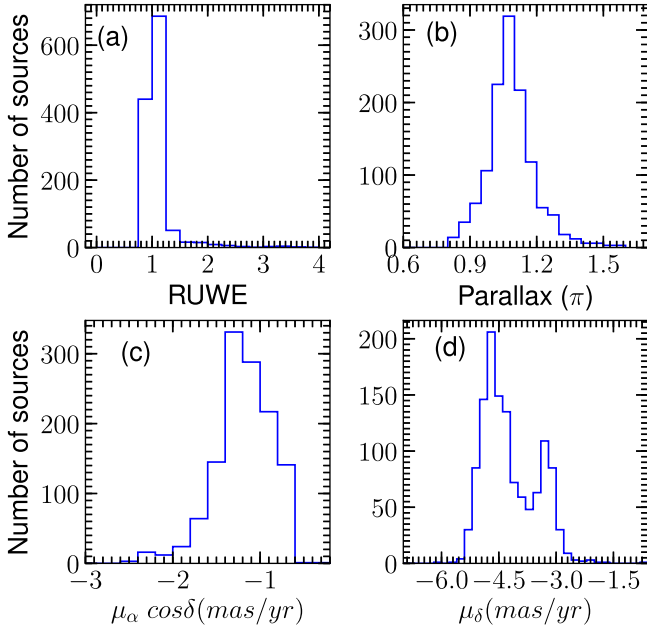


Figure 5. Histogram distributions of the RUWE (a), parallax (b), $\mu_\alpha \cos \delta$ (c), and μ_δ (d) of the 1243 member stars identified in this work. Bin sizes of the histograms are 0.25, 0.05 mas, 0.2 mas yr⁻¹, and 0.2 mas yr⁻¹, for the RUWE, parallax, $\mu_\alpha \cos \delta$, and μ_δ , respectively.

In our list of selected members, only 144 and 82 stars have $\text{RUWE} > 1.4$, from the list with $P_{\text{RF}} \geq 0.6$, and 0.8, respectively. These sources with higher RUWE could be multiple-star systems. The stars detected in this work are of good-quality sources. Out of the 1243 stars, $\sim 95\%$ of stars have a relative parallax error less than 20%.

Figure 5(b) displays the histogram distribution of parallaxes for all these identified member stars. In parallax, the stars detected in this work lie within a spread of ~ 0.8 mas with mean, median, and standard deviation values of 1.085 ± 0.003 mas, 1.078 mas, and 0.109 mas, respectively. The distance to the cluster is estimated using the parallax values of those sources whose relative parallax error ($\sigma \pi / \pi$) is better than 20% and $\text{RUWE} < 1.4$. Out of 1243, we find 1107 stars satisfy this condition. From these 1107 stars, we estimate the weighted mean parallax to be 1.090 ± 0.003 mas, which translates to a distance of 917 ± 2.7 pc. This distance estimate matches well with earlier estimates in literature (Contreras et al. 2002; Sicilia-Aguilar et al. 2019; Pelayo-Baldarrago et al. 2023).

In Figures 5(c) and (d), we show the histogram distributions of the proper motions ($\mu_\alpha \cos \delta$ and μ_δ). We derive the mean, median, and standard deviation values for $\mu_\alpha \cos \delta$ to be -1.194 ± 0.002 mas yr⁻¹, -1.187 mas yr⁻¹, and 0.325 mas yr⁻¹, respectively. For μ_δ , these values are -4.215 ± 0.004 mas yr⁻¹, -4.404 mas yr⁻¹, and 0.712 mas yr⁻¹, respectively.

3.4. Comparison with Literature

In this section, we compare our detected member stars with the sources detected in the literature. As discussed in Section 2.1, there are 1791 stars detected toward the complex based on various surveys. Also, using Gaia-DR2 data, Cantat-Gaudin et al. (2018) detected 460 stars toward IC 1396. We compare our findings separately with the source lists found in the literature.

To compare with the sources of various surveys, we first find their Gaia-DR3 counterpart information. Out of the 1791 stars, 1002 stars have Gaia counterparts. Then we refine the catalog further based on the astrometry quality. Thus, we use the 705 stars, which have a relative parallax error of $< 20\%$, for comparison. Of the 705 stars, 360 stars ($\sim 51\%$) are retrieved in our work as member stars with $P_{\text{RF}} \geq 0.8$. The number is 409 ($\sim 60\%$) with $P_{\text{RF}} \geq 0.6$. Due to their poor membership probability, the remaining stars are not detected as members.

Then we compare our member list with the 460 star list of Cantat-Gaudin et al. (2018). Within the common area, out of the 460 stars, we retrieved 348 ($\sim 76\%$) stars in this work with $P_{\text{RF}} \geq 0.8$. The number is 389 ($\sim 85\%$) with $P_{\text{RF}} \geq 0.6$. In this work, we consider only the stars with a higher probability of 80%. In Cantat-Gaudin et al. (2018), they considered all the stars with membership probability above 50%. So the stars, with higher probability, are retrieved in our work. In our work, we identify more member stars than Cantat-Gaudin et al. (2018) mainly due to the large area we consider.

Then we also compared the source list obtained by the various surveys (Section 2.1) with the stars detected by Cantat-Gaudin et al. (2018). Here, also we considered the good-quality 705 stars for comparison. In this case, we found 221 ($\sim 31\%$) survey-based stars common with the catalog of Cantat-Gaudin et al. (2018). There are 196 stars common to all three catalogs discussed here. We summarize the analysis as a Venn diagram (Figure 6).

4. Properties of the Complex

4.1. Subclusters within the Complex

The spatial distribution of the 1243 stars (Figure 4) displays the association of clustering with IC 1396. In this section, we attempt to identify the clusters quantitatively. To do this, we generate the surface density plot using the 1243 member stars and apply the nearest-neighbor (NN) method (Casertano & Hut 1985; Schmeja 2011). According to this method, the j th nearest-neighbor density is defined as

$$\rho_j = \frac{j-1}{S(r_j)}, \quad (1)$$

where r_j is the distance to its j th nearest neighbor and $S(r_j)$ is the surface area with radius r_j . To obtain the distribution of member stars, we use $j = 20$, which is found to be an optimum

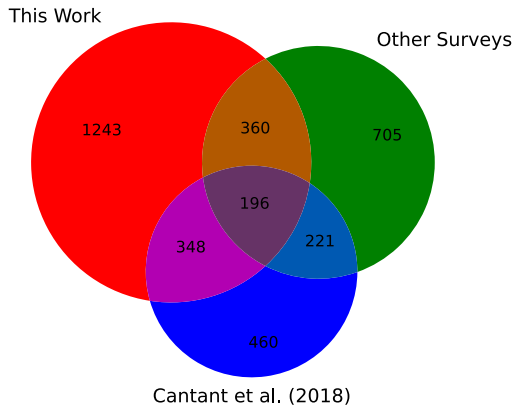


Figure 6. Venn diagram summarizing the comparison between the member population from this work with the stars from several other surveys and with stars from the work of Cantat-Gaudin et al. (2018).

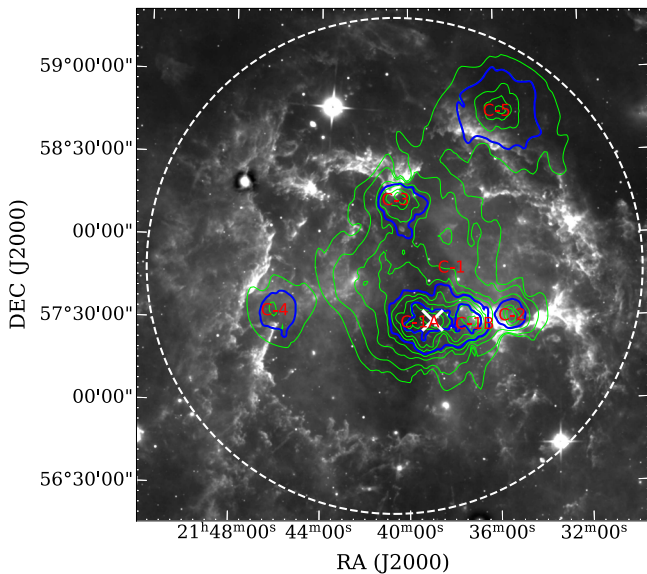


Figure 7. Contours of stellar surface density distribution generated using the 1243 candidate members identified toward IC 1396 complex overlaid on the WISE 22 μm band image. Contours are at levels of 0.6, 1, 2, 3, 5, 7, 10, 12, and 20 stars pc^{-2} . The white “x” symbol marks the position of the massive star HD 206267. Different clusters are retrieved from the stellar density map. The blue curves are the clusters shown along with their nomenclature.

value for cluster identification (Schmeja et al. 2008; Ramachandran et al. 2017; Damian et al. 2021). With this procedure, we generate the stellar density map with a pixel size of 0.1 pc ($20''/5$). Figure 7 shows the WISE 22 μm map overlaid with density contours. The lowest contour is at 0.6 stars pc^{-2} , within which the maximum number of sources falls. These stellar density contours reveal the cluster of stars toward the star-forming complex.

For the identification of the clusters in this region, we use the astrodendro algorithm (Robitaille et al. 2019) in Python. This algorithm works based on constructing tree structures starting from the brightest pixels in the data set and progressively adding fainter and fainter pixels. It requires the threshold flux value (minimum value), contour separation (min delta), and the minimum number of pixels required for a structure to be considered a cluster. In our analysis, we use the threshold and minimum delta to be 1.0 and 0.3 stars pc^{-2} , respectively. We

use the minimum number of pixels as 150 to detect the potential clusters. These parameters are adopted after multiple trials for the optimal detection of clusters. We identify six individual leaf structures with these input parameters, which we call clusters here. Two individual clusters (C-1A and C-1B) are seen toward the massive star HD 206267, and collectively (C-1) is the central cluster of this complex. Toward the tail of BRC IC 1396A, another grouping (C-2) of stars is also seen. Aside from this cluster toward the central part, another three clusters are also seen. They (C-3 and C-4) are linked to the BRC IC 1396N and SFO 39, respectively. We also detect a cluster (C-5) close to the boundary of the star-forming complex. Cluster identification in our work matches well with the clusters identified by Nakano et al. (2012) from the $\text{H}\alpha$ emission-line survey. In their work, a cluster is associated with the southern BRC SFO 37. However, in our analysis, we cannot see any such cluster with SFO 37, which could be due to the sensitivity of Gaia. The cluster (C-5), which we detect in this work, was not seen by Nakano et al. (2012), which could be because their work surveyed a smaller area than the area covered in this study.

In Table 4, we list the statistics (radius, number of stars, mean, median, and standard deviation) of the RUWE, parallax, $\mu_\alpha \cos \delta$, and μ_δ for all the identified clusters. We derive the physical radius ($R_{\text{cluster}} = (A_{\text{cluster}}/\pi)^{0.5}$; Das et al. 2017) of the clusters using the apertures retrieved from astrodendro. The area of each cluster is calculated as $A_{\text{cluster}} = N \times A_{\text{pixel}}$, where N is the number of pixels and A_{pixel} is the area of each pixel. The distribution of the parallax and the proper motions of the cluster stars are also displayed in Figure 8. We see from this plot two groupings. As we see, one is the larger group, mainly from the stars of the C-1 and C-2 clusters, and the second is a smaller group that appears due to stars from the other three (C-3, C-4, and C-5) clusters. This is also evident from the histogram distribution of μ_δ (Figure 5(d)). To quantitatively confirm our findings, we carry out a two-component Kolmogorov–Smirnov (KS) test with the parallax and proper motions. The p -score from the test is minimal and close to zero for the proper motions. For the parallax, the p -score is 0.02. This quantitatively confirms that proper-motion parameters are the distinctive astrometric features distinguishing the stars projected in the two subgroups, which is seen in Figure 8.

4.2. Age and Mass Range of the Candidate Cluster Members

In this section, we estimate the mean age and mass-completeness limit of the member stars identified in this analysis. Studies like Sicilia-Aguilar et al. (2005) and Getman et al. (2012) and references therein claim an approximate age of ~ 4 Myr for the primary cluster. To estimate the member population’s age and mass-completeness limit, we use the PARSEC isochrones available for the filters of Gaia-DR3 (Chen et al. 2014). We need to correct the isochrones for distance and extinction to fit them. In an earlier study using NIR and optical data, Sicilia-Aguilar et al. (2005) derived the average visual extinction value toward the entire complex to be $A_V = 1.5 \pm 0.5$ mag. This value also matches the estimations by Contreras et al. (2002) and Nakano et al. (2012). The majority of detected stars in this work are located toward the central part of IC 1396, which is expected to have less extinction due to the presence of massive star(s) around them compared to the surrounding regions such as BRCs, which are associated with dense molecular clouds. For further analysis, we use the

Table 4
The Number of Stars, Mean, Median, and Standard Deviation of the RUWE, Parallax, and Proper Motions of the Clusters Associated with IC 1396

Cluster	Radius (pc)	No. of Stars	RUWE			Parallax (mas)			$\mu_{\alpha} \cos \delta$ (mas yr ⁻¹)			μ_{δ} (mas yr ⁻¹)		
			Mean	Median	SD	Mean	Median	SD	Mean	Median	SD	Mean	Median	SD
			C-1	3.80	426	1.11	1.02	0.38	1.098 ± 0.006	1.084	0.118	-1.329 ± 0.004	-1.327	0.197
C-1A	1.72	162	1.11	1.02	0.37	1.101 ± 0.009	1.079	0.126	-1.298 ± 0.007	-1.309	0.159	-4.690 ± 0.010	-4.699	0.287
C-1B	1.22	80	1.12	1.02	0.53	1.108 ± 0.013	1.103	0.116	-1.442 ± 0.010	-1.449	0.222	-4.656 ± 0.016	-4.656	0.366
C-2	1.40	27	1.07	1.03	0.21	1.076 ± 0.026	1.066	0.102	-1.512 ± 0.019	-1.608	0.274	-4.825 ± 0.030	-4.882	0.411
C-3	2.17	60	1.11	1.02	0.38	1.047 ± 0.013	1.052	0.085	-1.172 ± 0.008	-1.117	0.317	-3.438 ± 0.014	-3.266	0.580
C-4	1.84	23	1.04	1.02	0.09	1.085 ± 0.021	1.080	0.097	-0.831 ± 0.014	-0.772	0.296	-3.332 ± 0.028	-3.417	0.225
C-5	3.76	87	1.07	1.02	0.12	1.083 ± 0.012	1.074	0.095	-0.854 ± 0.007	-0.816	0.141	-3.401 ± 0.013	-3.330	0.336

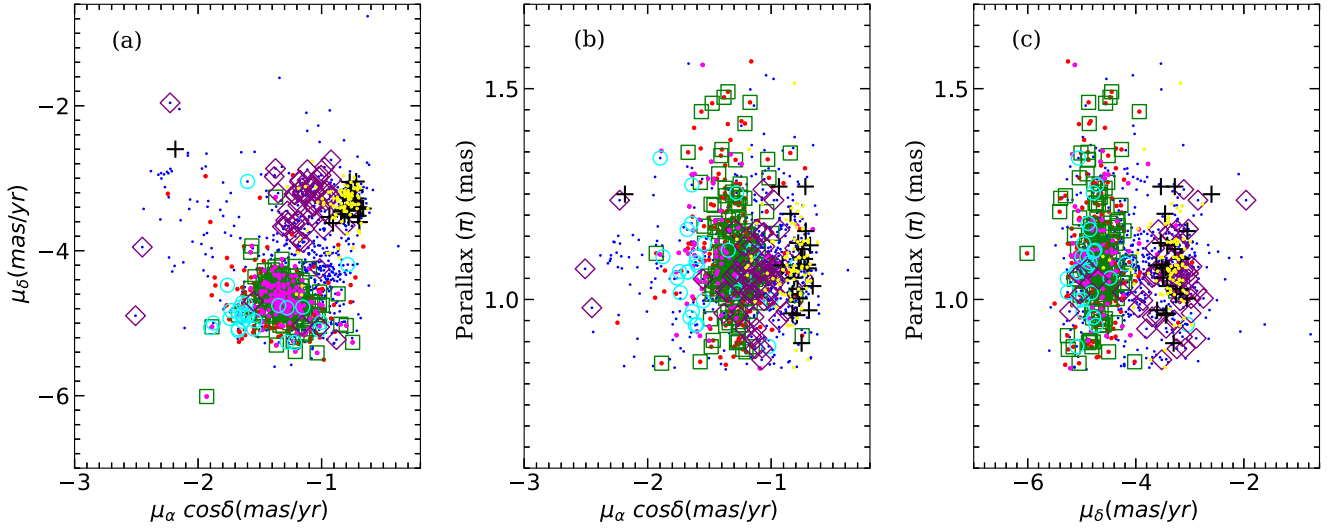


Figure 8. The spatial distribution of proper motions and parallax of the member stars detected in this work. Blue dots represent the 1243 member stars. The population of the clusters is shown in different colors and shapes. Clusters: C-1 (red dot), C-1A (green square), C-1B (magenta dot), C-2 (cyan circle), C-3 (purple diamond), C-4 (black plus mark), and C-5 (yellow dot).

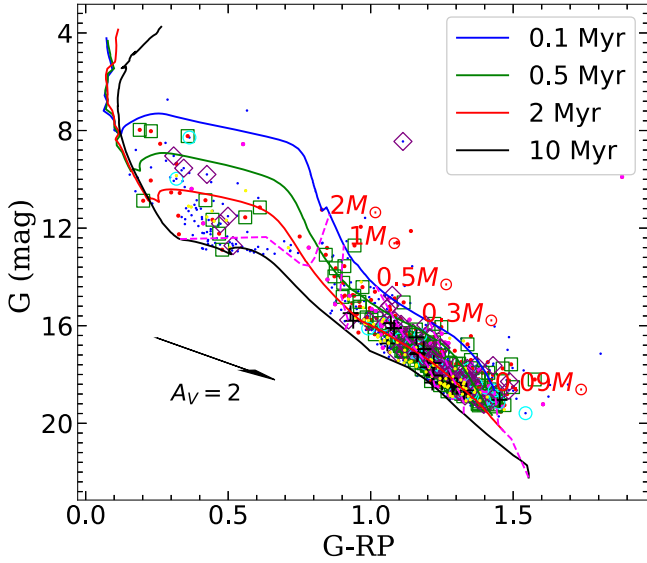


Figure 9. G vs. $G - RP$ CMD of the 1243 member stars within the IC 1396 complex. PARSEC isochrones of 0.1, 0.5, 2.0, and 10.0 Myr are overplotted. All the curves are plotted after correcting the distance (917 pc) and minimum extinction ($A_V = 1$ mag) (see text for details). Evolutionary tracks for stars having masses of 0.09, 0.3, 0.5, 1.0, and 2.0 M_\odot are also shown. The colored symbols have the same meaning as in Figure 8.

minimum extinction value of $A_V = 1$ mag obtained from Nakano et al. (2012).

After correcting for distance (917 pc) and extinction ($A_V = 1$ mag), we plot the isochrones of various ages on the G versus $G - RP$ CMD in Figure 9. To correct the extinction in individual bands for all the sources, we use the empirical relations of A_G/A_V and A_{RP}/A_V (Gaia Collaboration et al. 2018a; Bossini et al. 2019). In Figure 9, we plot various isochrones of evolutionary ages 0.1, 0.5, 2, and 10 Myr along with the evolutionary tracks corresponding to 0.09, 0.3, 0.5, 1, and 2 M_\odot . From Figure 9, we derive the age of individual stars by assigning the age of the closest isochrone. Similarly, by assigning the closest mass evolutionary track, we derive the

mass of individual stars. However, local variation in extinction and binarity of stars might affect the accurate estimation of these parameters. In Figure 10, we show the histogram distribution of the logarithmic values of the age. By fitting a Gaussian curve to the distribution, we obtain the mean logarithmic age of the cluster to be 6.17 ± 0.50 , which corresponds to a mean age of $\sim 1.5 \pm 1.6$ Myr. Using the upper limit of extinction, i.e., $A_V = 1.5$ mag, the mean age is obtained to be $\sim 1.6 \pm 1.7$ Myr, which still matches with the previous studies.

As discussed in Section 3.1, we see that the 90% completeness limits of G , BP, and RP bands are 20.5, 21.5, and 19.5 mag, respectively. We use the G -band to estimate the mass-completeness limit of the cluster. Using an extinction value of $A_V = 1-1.5$ mag and a distance of 917 pc, and considering a pre-main-sequence isochrone of 2 Myr (Chen et al. 2014), the magnitude limit of the G band (20.5 mag) corresponds to a mass of $\sim 0.1-0.2 M_\odot$. This analysis shows that Gaia-DR3 is complete down to the low-mass end. However, compared to the central region, i.e., toward the IC 1396A region, the extinction might be higher due to the presence of BRC and an associated molecular cloud. This local variation in extinction will play a role in the local mass completeness of the member stars toward the outer edge of the complex.

We list the mean, median, and standard deviation values of $\log(\text{age})$ and mass for the entire complex and the individual clusters in Table 5. The mean and median values of $\log(\text{age})$ and mass are similar, considering the whole complex and the clusters. This suggests that most of the population has evolved within a similar timescale of ~ 3 Myr. However, previous studies have shown that, in the proximity of BRC candidates, multi-episodic star formation is happening (Sicilia-Aguilar et al. 2014). Similarly, the stellar-mass distribution appears uniform for the entire complex, which can be seen from the mean and median values for all the clusters. However, local mass segregation might be happening within the individual clusters.

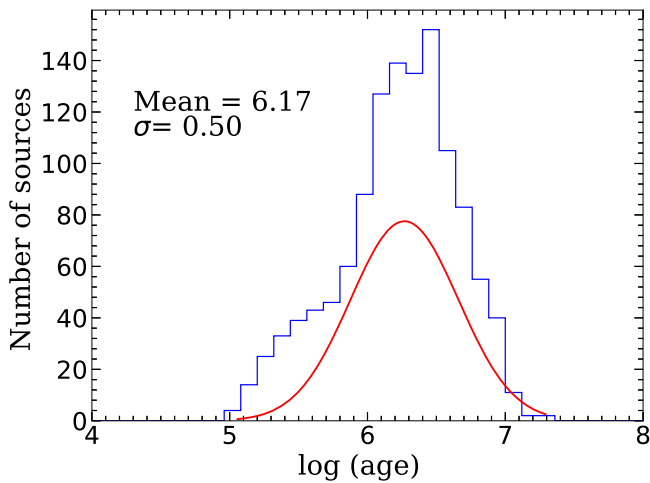


Figure 10. Histogram distribution of the logarithmic age of the 1243 candidate members of IC 1396. The red curve displays the Gaussian fit.

Table 5

Mean, Median, and Standard Deviation for Log(age) and Mass Derived from the Stars of the Entire IC 1396 and for the Clusters

Cluster	log(age)			Mass		
	(yr)			(M_{\odot})		
	Mean	Median	SD	Mean	Median	SD
Full	6.17	6.25	0.49	0.68	0.43	1.01
C-1	6.05	6.14	0.48	0.62	0.4	1.07
C-1A	6.06	6.14	0.49	0.70	0.4	1.37
C-1B	5.98	6.07	0.47	0.60	0.37	0.93
C-2	5.99	6.20	0.40	0.66	0.35	1.29
C-3	5.97	5.98	0.48	0.74	0.36	1.26
C-4	6.33	6.34	0.30	0.44	0.45	0.20
C-5	6.37	6.42	0.37	0.70	0.50	0.70

4.3. Cluster Properties

Several clusters have been identified toward IC 1396 based on the spatial distribution of the associated stellar members. Each cluster leaves an imprint of the ongoing star formation in the complex. In this section, we briefly discuss the formation of clusters taking into account their age and spatial distribution.

4.3.1. Inner Clusters (C-1 and C-2)

Clusters (C-1 and C-2) are located toward the center of the complex. Also, two subclusters (C-1A and C-1B) are observed within cluster C-1. Subcluster C-1A is on the eastern side, and C-1B is on the western side of the massive star. The subcluster C-1B is linked to the head of the BRC IC 1396A, while C-2 is seen toward its tail. C-1A contains more stars with slightly higher ages than C-1B. So the mean age of C-1A is slightly higher compared to C-1B. Similarly, the mean age of cluster C-2 is similar to C-1B. This indicates a multigeneration star formation triggered by the feedback effect of the central massive star. Earlier studies (Sicilia-Aguilar et al. 2014, 2019; Pelayo-Baldarrago et al. 2023) have reported such triggered star formation activities toward the head of IC 1396A. The presence of cluster C-2 is also a signature of ongoing triggered star formation toward the BRC complex. Using Herschel PACS images and analyzing the properties of young members in the head of IC 1396A, Sicilia-Aguilar et al. (2014) suggested that this second generation of star formation is triggered via

radiative-driven implosion (RDI) induced by the massive star HD 206267. However, more in-depth analysis with multi-wavelength data would be helpful to understand the mechanism behind the triggered star formation toward the entire IC 1396A region.

4.3.2. Outer Clusters (C-3, C-4, and C-5)

The outer clusters (C-3, C-4, and C-5) differ from the inner clusters based on their astrometry properties (see Figure 8). C-3 is linked with BRC IC 1396N, C-4 with SFO 37, and C-5 in the northwest boundary of IC 1396. The mean age of C-3 is slightly lower than C-1 (refer to Table 5). This indicates that the triggered star formation mechanism also forms the stars associated with IC 1396N. The mean age of C-4 and C-5 appears slightly higher than all other clusters. In these two clusters, a significant fraction of stars of higher age is present. Earlier studies carried out by Ikeda et al. (2008) and Panwar et al. (2014) have already reported sequential star formation in the direction of BRCs SFO 37 and SFO 39 (see Figure 1) due to the UV radiation impact of the exciting central star. The cluster C-4 is associated with SFO 39, but we do not detect any significant clustering toward SFO 37, as it is a small globule-like structure consisting of mainly a few embedded pre-main-sequence stars.

4.4. Radial Velocity

We searched for stars with radial-velocity (R_V) information in our member list. We obtained 107 stars with radial-velocity information from Gaia-DR3. This is an improvement in R_V measurements in the Gaia-DR3 catalog compared to the DR2 catalog. Out of these 107 stars, 85 stars with good astrometry quality, i.e., $\text{RUWE} < 1.4$, are considered for further analysis. The mean and median R_V of the 85 stars are -16.30 ± 1.28 and -16.56 km s^{-1} , respectively. To maximize the R_V measurements of the member stars of the complex, we also search for the R_V measurements in the literature. In previous work toward the region, Sicilia-Aguilar et al. (2006b) carried out high-resolution ($R \sim 34,000$) spectroscopic observations and obtained the radial-velocity information for 136 stars. By cross-matching these stars with our Gaia-detected member lists, we find 78 stars in common, out of which 67 stars are of good astrometry quality, i.e., $\text{RUWE} < 1.4$. The mean and median R_V of the 67 stars are -16.54 ± 0.25 and -15.80 km s^{-1} , respectively. The R_V has a broad range for the 85 stars compared to the list of 67 stars taken from Sicilia-Aguilar et al. (2006b). However, the mean and median values for both lists are similar. In Figure 11, we display the smooth histogram distribution for sources from both lists. In the figure, we scaled down the curve for the 67 stars by 50% for a better representation. The smoothed distribution from this figure also suggests similar mean and median values found from the different lists. The spatial distribution of these 152 stars with R_V information is shown in Figure 12. Most of the stars are distributed within the central part of the complex, with a few distributed all around the complex. Out of these 152 stars, 68 are members of the central cluster (C-1). We note that the properties of the complex and our identification of different subgroups in the complex are in close agreement with the recent work by Pelayo-Baldarrago et al. (2023).

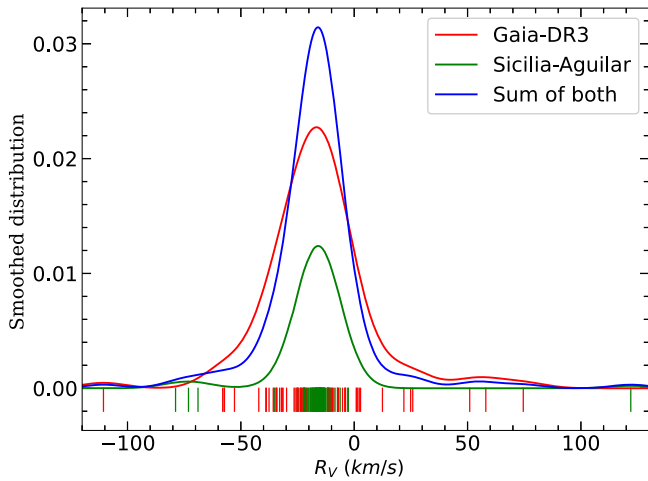


Figure 11. Smoothed histogram distribution of R_V values for the 85 stars (red), 67 stars (green), and the total 152 stars (blue). We have R_V values for 85 stars from Gaia-DR3. For the 67 stars, R_V values were taken from Sicilia-Aguilar et al. (2006b). To better represent the plot, the green curve is scaled down by 50%. The small vertical lines represent each star's R_V value.

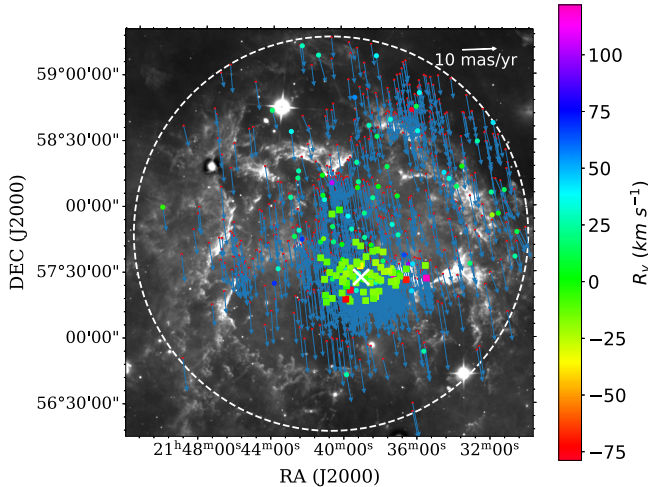


Figure 12. Spatial distribution of the 1243 member stars, shown as red dots, on the WISE 22 μm band. The proper-motion values are shown as arrows. A reference arrow of 10 mas yr^{-1} is shown in the top-right corner of the image. The 152 stars having R_V information are highlighted, where the 85 stars with Gaia-based R_V are shown as solid circles and the 67 sources from Sicilia-Aguilar et al. (2006b) are shown as square symbols. The colors of these objects mark their variation in R_V , which is displayed by the color bar.

5. Discussion

5.1. Kinematic Properties of IC 1396

In Figure 12, we show the spatial distribution of the 1243 stars on the WISE 22 μm band as red dots, along with their proper-motion values as blue arrows. The magnitudes of $\mu_\alpha \cos \delta$ and μ_δ give the length of the arrow and the signs of $\mu_\alpha \cos \delta$ and μ_δ determine the direction. All the arrows are scaled according to the white reference arrow of length 10 mas yr^{-1} . As seen from the plot, most stars are moving toward the south, one of the unique features observed toward the star-forming complex. In this section, we analyze the kinematics of the complex to shed more light on the internal motion of the member stars within the complex.

5.1.1. Determination of Three-dimensional Position and Velocity

Since the complex IC 1396 is a relatively large star-forming complex, it is essential to inspect its physical structure and spatial distribution in Galactic Cartesian coordinates, XYZ . We derive the XYZ coordinates for all the sources associated with IC 1396. The origin of the coordinate system is chosen to be the Sun. In this system, the X -axis runs along the Sun–Galactic center with a positive direction toward the Galactic center, and the Y -axis is in the Galactic plane orthogonal to the X -axis, with its positive direction along the Galactic rotation, the Z -axis is perpendicular to the Galactic plane, oriented in the direction of the Galactic North Pole. Thus, it makes a right-handed coordinate system. We used the Gaia-DR3 astrometric information of the detected stars and derived their three-dimensional positions (X, Y, Z) and the heliocentric velocities (U, V, W). We have also computed the LSR velocities for each star along with the heliocentric velocities. The transformation of heliocentric to LSR velocity considered the solar motion velocities ($U_0 = 11.1 \pm 0.7 \text{ km s}^{-1}$, $V_0 = 12.2 \pm 0.47 \text{ km s}^{-1}$, and $W_0 = 7.25 \pm 0.37 \text{ km s}^{-1}$) from Schönrich et al. (2010).

The majority of stars with R_V information lie toward the complex's central region. So, to obtain the kinematic property, we focus only on the central cluster C-1. Table 6 lists the derived 3D positions (X, Y, Z), the heliocentric velocities (U, V, W), and the LSR velocities of the 68 stars of the cluster C-1.

5.1.2. Kinematic Properties of the Stars

In Figure 13, we show the spatial distribution of the 68 stars of C-1, which have radial-velocity information in the XY , YZ , and XZ planes. In the top row, we display the heliocentric and LSR velocities. The heliocentric and LSR velocities indicate the stars' bulk motion.

To investigate the stability of the cluster C-1, it is essential to analyze the internal kinematics of the stars. First, we derive the mean value of the velocities of the stars. The values are listed in Table 7. To assess the internal motion of the stars, we calculate the difference in velocities ($\delta u, \delta v, \delta w$) of individual stars with respect to the mean value. In the bottom row of Figure 13, we show ($\delta u, \delta v, \delta w$). This displays the random movement of the stars with respect to the central velocity. This shows that the ($\delta u, \delta v, \delta w$) of stars are canceling each other, and the mean values of ($\delta u, \delta v, \delta w$) are close to zero, indicating no real expansion. The three-dimensional dispersion is $\sigma = \sqrt{(\sigma u)^2 + (\sigma v)^2 + (\sigma w)^2}$, derived to be 16.56 km s^{-1} .

Then we conduct a qualitative analysis of the relative motion of the stars within the complex in a similar manner carried out by Rivera et al. (2015) for the Taurus complex. This analysis will provide an implication of the stability of the complex. Each star is located at a certain distance from the complex's center and moves with a relative velocity. We denote the separation from the complex center with a position vector \mathbf{r}_* and the relative velocity vector as $\delta \mathbf{v}_*$. Each position vector is associated with a unit vector, which can be represented as $\hat{\mathbf{r}}_* = \mathbf{r}_*/|\mathbf{r}_*|$, directed from the center of complex toward the location of each star. So the relative motion of stars with respect to the complex center can be used to analyze the two types of motion: expansion or contraction and rotation. The expansion and contraction properties can be gauged by looking at the directions of the position vector and the relative velocity vector. For expansion, $\delta \mathbf{v}_*$ will be parallel to \mathbf{r}_* and for contraction $\delta \mathbf{v}_*$ will be antiparallel to \mathbf{r}_* . Hence, for

Table 6
3D Position, Heliocentric Velocities, and LSR Velocities of the 68 Stars within the Cluster C-1

Star No.	Source_ID	R.A. (2000) (degree)	Decl. (2000) (degree)	X (pc)	Y (pc)	Z (pc)	U (km s ⁻¹)	V (km s ⁻¹)	W (km s ⁻¹)	u (km s ⁻¹)	v (km s ⁻¹)	w (km s ⁻¹)	$\hat{r}_* \cdot \delta v_*$ (km s ⁻¹)	$\hat{r}_* \times \delta v_*$ (km s ⁻¹)		
1	2178383124508757120	325.1479	57.4754	-165.86	998.44	90.92	22.66	-18.99	-13.75	33.76	-6.75	-6.50	-5.02	-0.87	-0.16	1.19
2	2178384464538037376	324.8110	57.3874	-150.43	925.01	87.06	17.96	-6.24	-12.17	29.06	6.00	-4.92	-7.60	3.56	1.14	0.50
3	2178385942007271168	324.9923	57.4759	-142.16	861.63	83.00	19.24	-18.27	-12.72	30.34	-6.03	-5.47	3.72	-0.40	0.11	1.75
4	2178387556914944896	325.0083	57.5653	-170.96	1028.83	95.00	20.73	-54.06	-11.33	31.83	-41.82	-4.08	-38.90	3.59	0.29	-7.38
5	2178391989320655488	324.6100	57.4779	-135.03	832.29	83.10	16.58	-14.38	-11.84	27.68	-2.14	-4.59	-0.66	-0.90	0.10	3.83
6	2178394394502336768	324.5352	57.4465	-142.94	885.98	86.76	13.13	-10.52	-8.97	24.23	1.72	-1.72	-5.37	-3.48	-0.29	6.45
7	2178394531941271936	324.4657	57.4479	-143.82	894.13	87.71	18.56	-13.26	-10.34	29.66	-1.02	-3.09	-1.56	-2.31	-0.42	1.64
8	2178396868403779584	324.7432	57.4737	-145.45	891.47	86.29	21.12	-20.71	-14.08	32.22	-8.47	-6.83	6.49	0.79	0.15	0.34
9	2178397040202477952	324.7699	57.4714	-137.55	842.19	82.85	21.43	-30.57	-13.51	32.53	-18.33	-6.26	16.20	-0.46	0.05	1.60
10	2178397074562221952	324.8082	57.4760	-141.29	863.34	84.10	16.27	5.70	-11.68	27.37	17.94	-4.43	-20.46	0.53	0.17	1.10

(This table is available in its entirety in machine-readable form.)

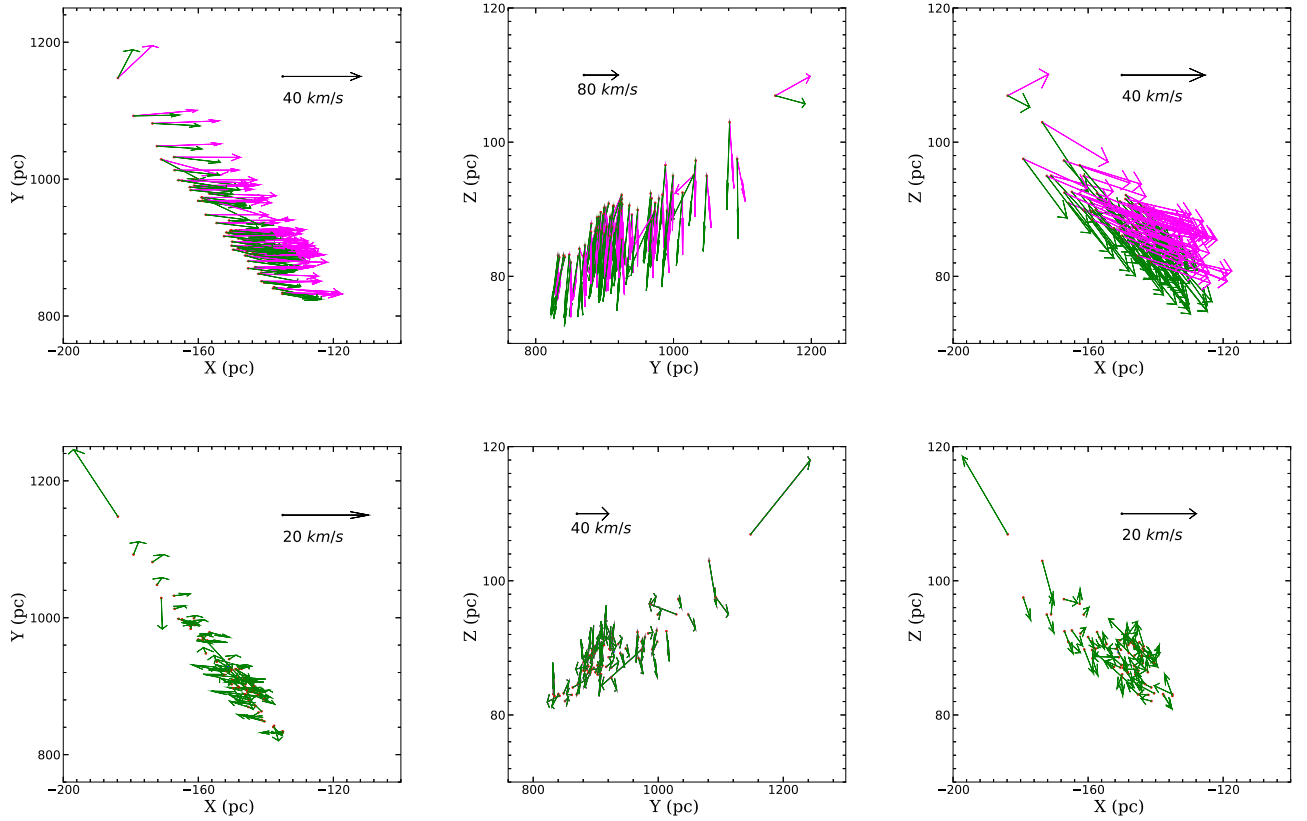


Figure 13. Spatial distribution of the 68 stars of C-1 on XY, YZ, and XZ planes. Top: arrows represent the heliocentric (green) and LSR (magenta) velocities of the 68 stars, respectively. Bottom: same as the top panel, but the arrows represent the difference between the individual velocities and mean velocity. Details of the velocities are given in the text.

expansion, the dot product ($\hat{r}_* \cdot \delta v_*$) should be a large and positive number, and for contraction, it should be a large and negative number. In a similar analogy, the cross-product ($\hat{r}_* \times \delta v_*$) will be small for both expansion and contraction. Inversely, the cross-product ($\hat{r}_* \times \delta v_*$) will be higher for large-scale rotation, and the dot product ($\hat{r}_* \cdot \delta v_*$) will be minimal.

In the following, we derive the dot and cross-products and list them in Table 6. Since in both the dot and cross-product parameters we use the unit position vector \hat{r}_* , the values of both parameters have similar velocities. The mean values of the parameters can be expressed with the equations $v_{\text{exp}} = \overline{\hat{r}_* \cdot \delta v_*}$ and $v_{\text{rot}} = \overline{\hat{r}_* \times \delta v_*}$.

We derive the expansion velocity, v_{exp} , to be 1.11 km s^{-1} . The derived rotation velocities are listed in Table 7. From CO maps, Patel et al. (1995) obtained the expansion velocity of the whole complex to be 5 km s^{-1} . Their analysis suggests that the gas within the complex is pushed away to the outskirts by the central massive star, resulting in an expansion of the system. A similar expansion velocity is also observed by Pelayo-Baldarrago et al. (2023). Though cluster C-1 is expanding, its expansion is slow compared to the whole complex. This could be because young stars dominate the central region, and cluster C-1 is expanding slowly due to higher density.

Nearby Galactic clusters are expanding with similar velocities to cluster C-1, observed by Kuhn et al. (2019). Their study over a set of 28 Galactic clusters using Gaia-DR2 reported a typical expansion velocity of $\sim 0.5 \text{ km s}^{-1}$. Similarly, the study conducted by Pang et al. (2021) of 13 open

clusters within a distance of 500 pc using Gaia-EDR3 reported many clusters to be supervirial and expanding in nature.

5.2. Star Formation History in IC 1396

IC 1396 is one of the nearby star-forming complexes dominated by feedback-driven star formation activity (see Section 2). The energetic stellar wind from the central massive star has cleared up most of the gas, resulting in a cavity of radius ~ 1.5 . The large cavity can be seen at infrared wavelengths with photodissociation regions (PDRs) associated with the boundary of the complex (see Figure 1). This massive feedback effect also forms BRCs and fingertip structures within the complex (Schwartz et al. 1991; Froebrich et al. 2005; Saurin et al. 2012). Here, we discuss the overall star formation history of the complex.

The spatial distribution of the member sources (see Figure 4) and their association with the BRCs all indicate the ongoing feedback-driven star formation activity within the complex. The mean age of the subclusters (see Section 4.2) suggests a multigeneration star formation activity within the complex. However, the formation of subclusters in the complex might have happened through a hierarchical process. To assess this nature, we conduct a KS test on the age of the two major groups of stars (see Section 4.1). One group is from the inner clusters (C-1 and C-2), and the other is from the outer clusters (C-3, C-4, and C-5). The p -score of the KS test comes out to be 0.00026. This low p -score value indicates that a majority number of stars from both groups might have formed over a similar timescale. The hierarchical star formation could be due

Table 7
Mean Values of Heliocentric and LSR Velocities and Dispersions Derived from the 68 Stars of Cluster C-1

Cluster	\bar{U} (km s ⁻¹)	\bar{V} (km s ⁻¹)	\bar{W} (km s ⁻¹)	\bar{u} (km s ⁻¹)	\bar{v} (km s ⁻¹)	\bar{w} (km s ⁻¹)	σu (km s ⁻¹)	σv (km s ⁻¹)	σw (km s ⁻¹)	σ (km s ⁻¹)	v_{exp} (km s ⁻¹)	v_{rot}^a (km s ⁻¹)		
C-1	20.47	-14.33	-12.75	32.57	-2.09	-5.50	3.04	16.15	2.03	16.56	1.11	-0.06	0.07	1.02

Note. Values of expansion and rotational velocities are listed in the table.

^a Columns 13, 14, and 15 list the values of the three components of the rotation velocity.

to the fractal and turbulent nature of the ambient cloud, where star formation can occur simultaneously or near-simultaneously at different locations of the clouds (Bonnell et al. 2003; Grudić et al. 2018; Tornamenti et al. 2022). However, one limitation of our analysis is that we have probed stars using optical measurements. Thus, many sources embedded in the BRCs might be missing in our analysis; as a result, the estimated ages of the groups associated with BRCs are likely upper limits.

Kinematics and age analysis of the embedded members are needed to understand whether the groups associated with BRCs are formed through entirely hierarchical collapse processes or whether stellar feedback from the central cluster has helped induce star formation in these clouds. In favorable conditions, stellar feedback can enhance or accelerate star formation in preexisting clouds where star formation is already underway. In this case, one may have both older as well as the young population of sources. Observations show that young clusters tend to show typical velocity dispersion of 2 km s^{-1} (Kuhn et al. 2019). Thus, older stars can move $\sim 2 \text{ pc}$ in 2 Myr of time, so inferences such as age gradient and elongated morphology, which are signatures of induced star formation as we move from ionizing sources to the tip of the BRCs, can be erased, particularly, if we are dealing with smaller groups or number of stars. Thus, compressive spectroscopic and kinematic analysis of member stars in both the optical and infrared bands would be highly desirable to shed more light on the formation of different subgroups in the complex.

6. Summary

We use the high-precision Gaia-DR3 astrometry and photometry data and apply machine-learning algorithms to carry out the membership analysis of the complex. Using the identified members in this work, we study various star formation properties of this complex. In the following, we report our significant findings from this work.

1. Using Gaia-DR3 astrometry and photometry data and applying the supervised RF technique from the machine-learning algorithm, we identify this complex's 1243 high-probability member population. The identified member population is of high quality, with 95% of stars having a relative parallax error of less than 20%. More than 99% of stars have a RUWE less than 1.4, suggesting they are of high astrometry quality. Of the 1243 stars, 731 are entirely new members identified in this work. This has significantly enhanced the reliable member population list for IC 1396.
2. The mean values of the parameters RUWE, parallax, $\mu_\alpha \cos \delta$, and μ_δ are 1.12, $1.085 \pm 0.003 \text{ mas}$, $-1.194 \pm 0.002 \text{ mas yr}^{-1}$, and $-4.215 \pm 0.004 \text{ mas yr}^{-1}$, respectively. The spatial distribution of the parallax, $\mu_\alpha \cos \delta$, and μ_δ suggests that the total population is broadly segregated into two groups. Our KS test shows that proper-motion parameters are the most distinctive astrometric features, distinguishing the stars projected in the two subgroups.
3. The spatial distribution of the stars reveals the associated clusters. We use the NN method to identify six clusters (#C-1A, C-1B, C-2, C-3, C-4, and C-5) toward IC 1396. C-1A and C-1B are the subclusters of the central cluster C-1. We study the statistical properties of stars lying within the subclusters.

4. Using the G versus $G - RP$ CMD and parsec isochrones, we estimate the age and mass of individual stars. The mean age derived from all 1243 stars is $1.5 \pm 1.6 \text{ Myr}$, matching the estimations from previous studies. Using the completeness limit of 19 mag in the G band and distance to be 917 pc, we derive the mass-completeness limit for the complex to be $\sim 0.1 M_\odot$. Thus suggesting the complex is associated very low massive population.
5. Of the 1243 stars, 152 good-quality stars ($\text{RUWE} < 1.4$) have R_V measurements, out of which 85 stars have R_V information from Gaia-DR3 and the remaining 67 stars from a high-resolution spectroscopic study of Sicilia-Aguilar et al. (2006b). The mean and median values of R_V derived from the 152 stars are -16.41 ± 0.72 and 15.80 km s^{-1} , respectively.
6. We carry out a 3D kinematic analysis to understand the internal motion of stars within the central cluster C-1. We use the R_V values and astrometric data of the 68 stars of the cluster. We derive the 3D Cartesian position and velocities of each star. To study the stability of the cluster, we derive the expansion velocity, which is low compared to the previous value derived from CO maps. The low value of the expansion velocity of the cluster suggests a slow expansion compared to the whole complex. The slow expansion might be due to the higher density of the recently formed young stars.
7. Considering the spatial distribution, association with BRCs, and age of the stars, we study the overall star formation within the complex. The variation in the age of the subclusters suggests an ongoing multigeneration star formation process in the complex. However, the subclusters of the complex might have formed through a hierarchical process.

We thank the anonymous referee for a constructive review of the manuscript, which helped in improving the quality of the paper. S.R.D. acknowledges support from Fondecyt Postdoctoral fellowship (project code 3220162). This work presents results from the European Space Agency (ESA) space mission Gaia. Gaia data are being processed by the Gaia Data Processing and Analysis Consortium (DPAC). Funding for the DPAC is provided by national institutions, in particular the institutions participating in the Gaia MultiLateral Agreement (MLA). The Gaia mission website is <https://www.cosmos.esa.int/gaia>. The Gaia archive website is <https://archives.esac.esa.int/gaia>. This publication makes use of data products from the Wide-field Infrared Survey Explorer, which is a joint project of the University of California, Los Angeles, and the Jet Propulsion Laboratory/California Institute of Technology, funded by the National Aeronautics and Space Administration. This research has made use of the SIMBAD database, operated at CDS, Strasbourg, France.

Software: Astropy (Astropy Collaboration et al. 2013), APLpy (Robitaille & Bressert 2012; Robitaille 2019), Scikit-learn (Pedregosa et al. 2011), Matplotlib (Hunter 2007), NumPy (Harris et al. 2020), Pandas (McKinney 2010).

Appendix A Gaussian Mixture Model

GMM works on the simple principle of identifying the normally distributed subpopulations from the overall population. This model assumes that the data points are generated

from a mixture of a finite number of Gaussian distributions with unknown parameters. In the GMM method, each data point will be categorized into cluster members or nonmembers, depending on its membership score (probability). The mixture models do not require prior knowledge of classifying subpopulations. This allows the model to learn the subpopulation in an automated way. Since there is no previous knowledge of the subpopulation assignment, this mixture model constitutes unsupervised machine learning. This technique is widely used in various fields, including astrophysics (Lee et al. 2012; Igoshev & Popov 2013; Zhang et al. 2016; Chattopadhyay & Maitra 2017; Holoien et al. 2017; Gao 2018a, 2018b; Kaplan et al. 2018). Below we briefly describe the working principle of the GMM method.

If there are m clusters present in n -dimensional parameter space, then the probability distribution $P(x)$ of a data x is estimated as the weighted summation of all the m Gaussian components:

$$P(x) = \sum_{k=1}^m w_k P(x | \mu_k, \Sigma_k), \quad (\text{A1})$$

where Σ_k is the covariance matrix and w_k is the mixture weight of the k th Gaussian component, which satisfies the condition $\sum_{k=1}^m w_k = 1$. The distribution of individual Gaussian cluster is

$$P(x | \mu_k, \Sigma_k) = \frac{\exp\left[-\frac{1}{2}(x - \mu_k)\Sigma_k^{-1}(x - \mu_k)\right]}{(2\pi)^{n/2}\sqrt{|\Sigma_k|}}, \quad (\text{A2})$$

where μ_k and Σ_k are the mean vector and covariance matrix of the k th Gaussian component. $|\Sigma_k|$ is the determinant of Σ_k .

In GMM, the parameters w_k , μ_k , and Σ_k are determined using the unsupervised machine-learning technique, known as the expectation-maximization (EM) algorithm (Dempster et al. 1977; Press et al. 2007). The maximum likelihood of the data strictly increases with each subsequent iteration, which implies that it is guaranteed to approach a local maximum. This algorithm does not assume any prior knowledge about clustering structures. The EM algorithm starts with an initial guess for N data points and learns the GMM parameters from the data. This process involves a few steps, which is described in detail in Lee et al. (2012). After calculating the distribution parameters, the distribution probability $P(x|\mu_k, \Sigma_k)$ for each data point x can be estimated.

Before carrying out the clustering analysis, it is essential to normalize the data. This data normalization is often required for similarity measures (e.g., Euclidean distance), which are sensitive to the differences in magnitudes or scales (Gao 2018a, 2018b). In our case, we have done the data normalization following the discussions made in Gao (2018b). If N stars have an n -dimensional parameter space, the normalized parameter in the j th dimension X_i^j is defined as

$$X_i^j = \frac{x_i^j - \text{Med}(x^j)}{\sigma x^j}, \quad (\text{A3})$$

where x_i^j the original parameter, $\text{Med}(x^j)$ is the median of x^j distribution, and σx^j is its standard deviation.

Appendix B Random-forest Classifier Efficiency

As explained in Section 3.2.1, within a small circular area of radius $30'$, we find 577 stars as probable members and 2503

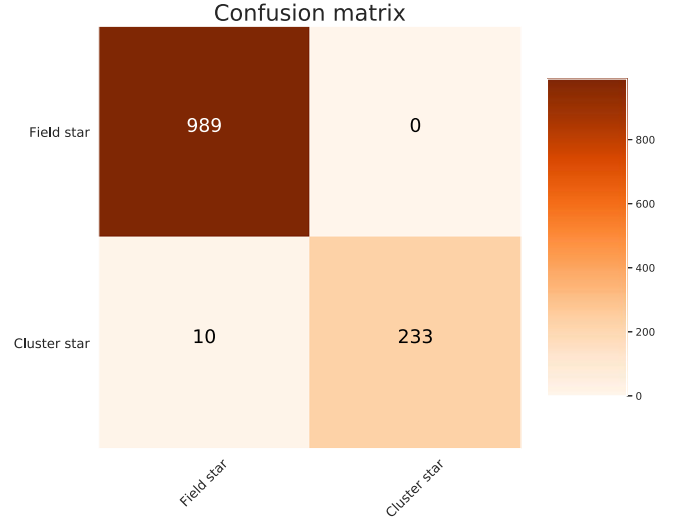


Figure 14. Confusion matrix generated by the RF method. The cluster stars and field stars are displayed in the plot.

Table 8
Relative Importance of the 11 Input Parameters

Parameter	Relative Importance
R.A.	0.010
Decl.	0.009
Parallax	0.027
$\mu_\alpha \cos \delta$	0.172
μ_δ	0.128
G -mag	0.102
BP-mag	0.051
RP-mag	0.138
BP – RP	0.140
BP – G	0.169
G – RP	0.052

stars to be nonmembers. Using this result of GMM, we construct a reliable training set. This is quite important since the RF method is highly dependent on the training set. Since RF is handy in handling large dimensions, we use 11 input parameters in this work. The input parameters set include five position parameters: coordinates, proper motions, parallax, and six photometric parameters such as magnitudes in the G band, BP band, RP band, $BP - RP$ color, and $BP - G$ and $G - RP$ color. Hence, we construct the RF classifier using the one-dimensional reliable training set and test its accuracy. For this purpose, we use 60% of the input 3080 stars to train the RF classifier and the remaining 40% of data to test the accuracy. So in our case, out of 3080 stars, 1848 stars are used to train the RF method, and the remaining 1232 stars are used to test how well the machine gets trained in recognizing the member stars and the field stars. The machine itself randomly chooses the training and test sets. We obtain a high accuracy of 0.99 while running the RF method over the test data set. The confusion matrix shown in Figure 14 presents the RF method's high accuracy. This confusion matrix shows how the machine identifies the sources based on training. As can be deduced from the confusion matrix, out of 1232 sources used to test the machine's accuracy, the machine successfully identified 989 nonmember or field stars and 233 cluster member stars. The machine is confused, with only a few field and cluster member

stars during classification. This exercise demonstrates the effectiveness of the RF method.

Table 8 provides the relative importance of 11 input parameters found by RF while providing the membership probability. We see that the proper motion in RA ($\mu_\alpha \cos \delta$) has maximum relative importance in membership identification compared to other parameters. The proper motion in dec (μ_δ) also has relatively high importance in segregating member and nonmember stars. However, in our case, the color terms ($BP - G$ and $BP - RP$) and the magnitude ($RP - \text{mag}$) get higher importance in correctly identifying members and nonmembers. The reason is due to the filtering of stars using CMDs during the GMM method (see Section 3.2.1). Usually, proper motions play a dominant role in cluster identification; in our case, we also observe the same. The coordinates of the stars (R.A., decl.) have minor importance in membership identification. In previous analyses, Gao (2018a, 2018b) also obtain a similar result in the regions of NGC 6405 and M67. It is worth

mentioning here that while running RF, there is no need for data normalization as was done for the GMM method.

Appendix C CMD Plots of Stars with $P_{\text{RF}} \leq 0.5$

Generally, stars with $P_{\text{RF}} < 50\%$ are nonmember stars. Here in Figure 15, we show the CMDs of stars retrieved with $P_{\text{RF}} < 50\%$ and G band less than 19 mag. Stars lying within different P_{RF} values are shown here. This is to check their location on the CMD. Out of the total stars with $P_{\text{RF}} < 50\%$ and G mag less than 19, the majority (70%) stars lie within $P_{\text{RF}} < 10\%$. The stars with $P_{\text{RF}} < 1\%$ are the most likely nonmember. However, stars with higher probability are spread on the plot. This discussion aims to shed light on the nature of stars with different probabilities. This is to stress the fact that member and nonmember stars should be chosen carefully in this type of membership analysis, where the magnitude and color terms will play a major role in segregating member and

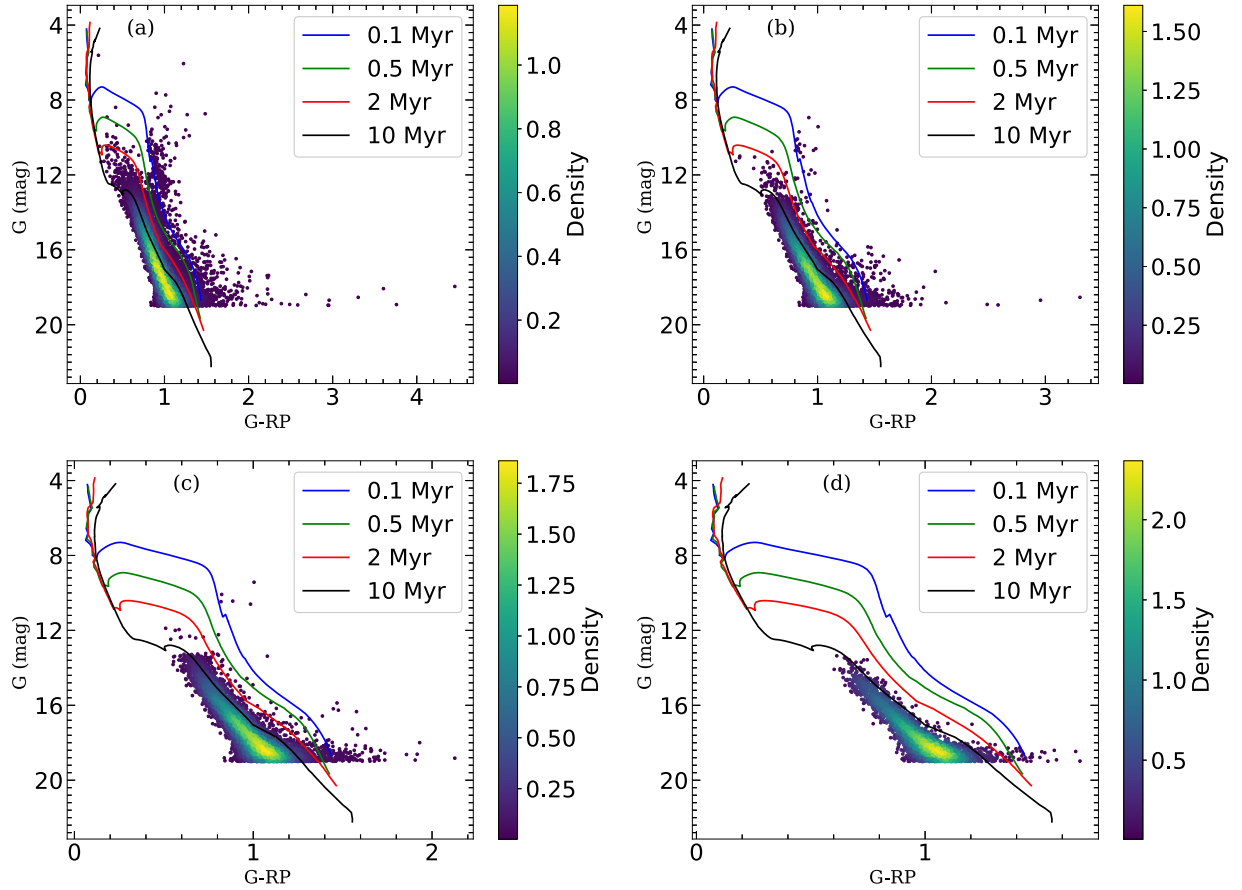


Figure 15. Same as Figure 9, but for the stars with $P_{\text{RF}} \leq 50\%$ and G band less than 19 mag. (a) All stars and (b), (c), and (d) for stars with $P_{\text{RF}} \leq 10\%$, 5% , and 1% , respectively. The color bar displays the variation in the density distribution of sources.

nonmember stars. An overlap in the magnitude and color terms of both member and nonmember stars will lead to the failure of effective training of the machine.

ORCID iDs

Swagat R. Das  <https://orcid.org/0000-0001-7151-0882>

Manash Samal  <https://orcid.org/0000-0002-9431-6297>

Jessy Jose  <https://orcid.org/0000-0003-4908-4404>

References

- Astropy Collaboration, Robitaille, T. P., & Tollerud, E. J. 2013, *A&A*, **558**, A33
- Balaguer-Núñez, L., Galadí-Enríquez, D., & Jordi, C. 2007, *A&A*, **470**, 585
- Barentsen, G., Vink, J. S., Drew, J. E., et al. 2011, *MNRAS*, **415**, 103
- Bastian, N., Adamo, A., Gieles, M., et al. 2012, *MNRAS*, **419**, 2606
- Blaauw, A. 1964, *ARA&A*, **2**, 213
- Bonnell, I. A., Bate, M. R., & Vine, S. G. 2003, *MNRAS*, **343**, 413
- Bonnell, I. A., Clark, P., & Bate, M. R. 2008, *MNRAS*, **389**, 1556
- Bossini, D., Vallenari, A., Bragaglia, A., et al. 2019, *A&A*, **623**, A108
- Brandt, T. D. 2021, *ApJS*, **254**, 42
- Breiman, L. 2001, *Machine Learning*, 45, 5
- Brink, H., Richards, J. W., Poznanski, D., et al. 2013, *MNRAS*, **435**, 1047
- Cabrera-Cano, J., & Alfaro, E. J. 1990, *A&A*, **235**, 94
- Cantat-Gaudin, T., Jordi, C., Vallenari, A., et al. 2018, *A&A*, **618**, A93
- Casertano, S., & Hut, P. 1985, *ApJ*, **298**, 80
- Chattopadhyay, S., & Maitra, R. 2017, *MNRAS*, **469**, 3374
- Chen, Y., Girardi, L., Bressan, A., et al. 2014, *MNRAS*, **444**, 2525
- Choudhury, R., Mookerjee, B., & Bhatt, H. C. 2010, *ApJ*, **717**, 1067
- Clarke, C. J., Bonnell, I. A., & Hillenbrand, L. A. 2000, in *Protostars and Planets IV*, ed. V. Mannings, A. P. Boss, & S. S. Russell (Tucson, AZ: Univ. Arizona Press), 151
- Contreras, M. E., Sicilia-Aguilar, A., Muzerolle, J., et al. 2002, *AJ*, **124**, 1585
- Dale, J. E., Ercolano, B., & Bonnell, I. A. 2012, *MNRAS*, **424**, 377
- Dale, J. E., Ercolano, B., & Bonnell, I. A. 2013, *MNRAS*, **430**, 234
- Damian, B., Jose, J., Samal, M. R., et al. 2021, *MNRAS*, **504**, 2557
- Das, S. R., Jose, J., Samal, M. R., Zhang, S., & Panwar, N. 2021, *MNRAS*, **500**, 3123
- Das, S. R., Tej, A., Vig, S., et al. 2017, *MNRAS*, **472**, 4750
- de Zeeuw, P. T., Hoogerwerf, R., de Bruijne, J. H. J., Brown, A. G. A., & Blaauw, A. 1999, *AJ*, **117**, 354
- Deacon, N. R., & Hambly, N. C. 2004, *A&A*, **416**, 125
- Dempster, A. P., Laird, N. M., & Rubin, D. B. 1977, *J. R. Stat. Soc. B*, **39**, 1
- Dubath, P., Rimoldini, L., Süveges, M., et al. 2011, *MNRAS*, **414**, 2602
- Elmegreen, B. G. 1983, *MNRAS*, **203**, 1011
- Elmegreen, B. G., & Scalo, J. 2004, *ARA&A*, **42**, 211
- Ferraro, F. R., Massari, D., Dalessandro, E., et al. 2016, *ApJ*, **828**, 75
- Froebich, D., Scholz, A., Eislöffel, J., & Murphy, G. C. 2005, *A&A*, **432**, 575
- Gaia Collaboration 2022, Gaia DR3, Version 1.0, doi:10.5270/esa-qa4lep3
- Gaia Collaboration, Babusiaux, C., & van Leeuwen, F. 2018a, *A&A*, **616**, A10
- Gaia Collaboration, Brown, A. G. A., Vallenari, A., et al. 2018b, *A&A*, **616**, A1
- Gaia Collaboration, Brown, A. G. A., & Vallenari, A. 2021, *A&A*, **649**, A1
- Gaia Collaboration, Helmi, A., & van Leeuwen, F. 2018c, *A&A*, **616**, A12
- Gaia Collaboration, Prusti, T., de Bruijne, J. H. J., et al. 2016, *A&A*, **595**, A1
- Galli, P. A. B., Bouy, H., Olivares, J., et al. 2020, *A&A*, **643**, A148
- Galli, P. A. B., Bouy, H., Olivares, J., et al. 2021, *A&A*, **646**, A46
- Gao, X. 2018a, *ApJ*, **869**, 9
- Gao, X. 2018b, *AJ*, **156**, 121
- Getman, K. V., Broos, P. S., Kuhn, M. A., et al. 2017, *ApJS*, **229**, 28
- Getman, K. V., Feigelson, E. D., Garmire, G., Broos, P., & Wang, J. 2007, *ApJ*, **654**, 316
- Getman, K. V., Feigelson, E. D., Sicilia-Aguilar, A., et al. 2012, *MNRAS*, **426**, 2917
- Gieles, M., & Portegies Zwart, S. F. 2011, *MNRAS*, **410**, L6
- Grudić, M. Y., Guszejnov, D., Hopkins, P. F., et al. 2018, *MNRAS*, **481**, 688
- Gupta, S., Jose, J., More, S., et al. 2021, *MNRAS*, **508**, 3388
- Harris, C. R., Millman, K. J., van der Walt, S. J., et al. 2020, *Natur*, **585**, 357
- Holoien, T. W. S., Marshall, P. J., & Wechsler, R. H. 2017, *AJ*, **153**, 249
- Hunter, J. D. 2007, *CSE*, **9**, 90
- Igoshev, A. P., & Popov, S. B. 2013, *MNRAS*, **434**, 2229
- Ikeda, H., Sugitani, K., Watanabe, M., et al. 2008, *AJ*, **135**, 2323
- Jose, J., Herczeg, G. J., Samal, M. R., Fang, Q., & Panwar, N. 2017, *ApJ*, **836**, 98
- Jose, J., Kim, J. S., Herczeg, G. J., et al. 2016, *ApJ*, **822**, 49
- Jose, J., Pandey, A. K., Samal, M. R., et al. 2013, *MNRAS*, **432**, 3445
- Kaplan, D. L., Swiggum, J. K., Fichtenbauer, T. D. J., & Vallisneri, M. 2018, *ApJ*, **855**, 14
- Karnath, N., Prchlik, J. J., Gutermuth, R. A., et al. 2019, *ApJ*, **871**, 46
- Koposov, S. E., Belokurov, V., & Torrealba, G. 2017, *MNRAS*, **470**, 2702
- Kozhurina-Platais, V., Girard, T. M., Platais, I., et al. 1995, *AJ*, **109**, 672
- Krone-Martins, A., & Moitinho, A. 2014, *A&A*, **561**, A57
- Kroupa, P. 2008, in *IAU Symp. 246, Dynamical Evolution of Dense Stellar Systems*, ed. E. Vesperini, M. Giersz, & A. Sills (Cambridge: Cambridge Univ. Press), 13
- Kuhn, M. A., Hillenbrand, L. A., Sills, A., Feigelson, E. D., & Getman, K. V. 2019, *ApJ*, **870**, 32
- Lada, C. J. 1987, in *IAU Symp. 115, Star Forming Regions*, ed. M. Peimbert & J. Jugaku (Cambridge: Cambridge Univ. Press), 1
- Larson, R. B. 1981, *MNRAS*, **194**, 809
- Lee, K. J., Guillemot, L., Yue, Y. L., Kramer, M., & Champion, D. J. 2012, *MNRAS*, **424**, 2832
- Lin, H.-W., Chen, Y.-T., Wang, J.-H., et al. 2018, *PASJ*, **70**, S39
- Liu, C., Deng, N., Wang, J. T. L., & Wang, H. 2017, *ApJ*, **843**, 104
- Lodieu, N., Deacon, N. R., & Hambly, N. C. 2012, *MNRAS*, **422**, 1495
- Mac Low, M.-M., & Klessen, R. S. 2004, *RvMP*, **76**, 125
- Mahmudunnobe, M., Hasan, P., Raja, M., & Hasan, S. N. 2021, *EPJST*, **230**, 2177
- Maíz Apellániz, J., & Barbá, R. H. 2020, *A&A*, **636**, A28
- McKee, C. F., & Ostriker, E. C. 2007, *ARA&A*, **45**, 565
- McKinney, W. 2010, in *Proc. 9th Python in Science Conf.*, ed. S. van der Walt & J. Millman, 56
- Megeath, S. T., Allen, L. E., Gutermuth, R. A., et al. 2004, *ApJS*, **154**, 367
- Mercer, E. P., Miller, J. M., Calvet, N., et al. 2009, *AJ*, **138**, 7
- Morales-Calderón, M., Stauffer, J. R., Rebull, L., et al. 2009, *ApJ*, **702**, 1507
- Muzic, K., Almendros-Abad, V., Bouy, H., et al. 2022, *A&A*, **668**, A19
- Nakano, M., Sugitani, K., Watanabe, M., et al. 2012, *AJ*, **143**, 61
- Olivares, J., Bouy, H., Sarro, L. M., et al. 2019, *A&A*, **625**, A115
- Pandey, R., Sharma, S., Dewangan, L. K., et al. 2022, *ApJ*, **926**, 25
- Pang, X., Li, Y., Tang, S.-Y., Pasquato, M., & Kouwenhoven, M. B. N. 2020, *ApJL*, **900**, L4
- Pang, X., Li, Y., Yu, Z., et al. 2021, *ApJ*, **912**, 162
- Panwar, N., Chen, W. P., Pandey, A. K., et al. 2014, *MNRAS*, **443**, 1614
- Patel, N. A., Goldsmith, P. F., Snell, R. L., Hezel, T., & Xie, T. 1995, *ApJ*, **447**, 721
- Pedregosa, F., Varoquaux, G., Gramfort, A., et al. 2011, *JMLR*, **12**, 2825
- Pelayo-Baldarrago, M. E., Sicilia-Aguilar, A., Fang, M., et al. 2023, *A&A*, **669**, A22
- Peter, D., Feldt, M., Henning, T., & Hormuth, F. 2012, *A&A*, **538**, A74
- Platais, I. 1991, *A&AS*, **87**, 69
- Plewa, P. M. 2018, *MNRAS*, **476**, 3974
- Portegies Zwart, S. F., McMillan, S. L. W., & Gieles, M. 2010, *ARA&A*, **48**, 431
- Press, W., Teukolsky, S., Vetterling, W., & Flannery, B. 2007, *Numerical Recipes: The Art of Scientific Computing* (3rd ed.; Cambridge: Cambridge Univ. Press)
- Ramachandran, V., Das, S. R., Tej, A., et al. 2017, *MNRAS*, **465**, 4753
- Reach, W. T., Rho, J., Young, E., et al. 2004, *ApJS*, **154**, 385
- Rivera, J. L., Loinard, L., Dzib, S. A., et al. 2015, *ApJ*, **807**, 119
- Robitaille, T. 2019, *APLpy v2.0: The Astronomical Plotting Library in Python, 2.0*, Zenodo, doi:10.5281/zenodo.2567476
- Robitaille, T., & Bressert, E. 2012, *APLpy: Astronomical Plotting Library in Python*, Astrophysics Source Code Library, ascl:1208.017
- Robitaille, T., Rice, T., Beaumont, C., et al. 2019, *astrodendro: Astronomical Data Rendering Creator*, Astrophysics Source Code Library, ascl:1907.016
- Samal, M. R., Zavagno, A., Deharveng, L., et al. 2014, *A&A*, **566**, A122
- Sanders, W. L. 1971, *A&A*, **14**, 226
- Sarro, L. M., Bouy, H., Berihuete, A., et al. 2014, *A&A*, **563**, A45
- Saurin, T. A., Bica, E., & Bonatto, C. 2012, *MNRAS*, **421**, 3206
- Schmeja, S. 2011, *AN*, **332**, 172
- Schmeja, S., Kumar, M. S. N., & Ferreira, B. 2008, *MNRAS*, **389**, 1209
- Schönrich, R., Binney, J., & Dehnen, W. 2010, *MNRAS*, **403**, 1829
- Schwartz, R. D., Wilking, B. A., & Giullbudagian, A. L. 1991, *ApJ*, **370**, 263
- Sicilia-Aguilar, A., Hartmann, L., Calvet, N., et al. 2006a, *ApJ*, **638**, 897
- Sicilia-Aguilar, A., Hartmann, L. W., Briceño, C., Muzerolle, J., & Calvet, N. 2004, *AJ*, **128**, 805

- Sicilia-Aguilar, A., Hartmann, L. W., Fűrész, G., et al. 2006b, [AJ](#), **132**, 2135
- Sicilia-Aguilar, A., Hartmann, L. W., Hernández, J., Briceño, C., & Calvet, N. 2005, [AJ](#), **130**, 188
- Sicilia-Aguilar, A., Kim, J. S., Sobolev, A., et al. 2013, [A&A](#), **559**, A3
- Sicilia-Aguilar, A., Patel, N., Fang, M., et al. 2019, [A&A](#), **622**, A118
- Sicilia-Aguilar, A., Roccatagliata, V., Getman, K., et al. 2014, [A&A](#), **562**, A131
- Sicilia-Aguilar, A., Roccatagliata, V., Getman, K., et al. 2015, [A&A](#), **573**, A19
- Silverberg, S. M., Günther, H. M., Kim, J. S., Principe, D. A., & Wolk, S. J. 2021, [AJ](#), **162**, 279
- Stickland, D. J. 1995, *Obs*, **115**, 180
- Sugitani, K., Fukui, Y., & Ogura, K. 1991, [ApJS](#), **77**, 59
- Tornamenti, S., Pasquato, M., Di Cintio, P., et al. 2022, [MNRAS](#), **510**, 2097
- Trumpler, R. J. 1930, [LicOB](#), **420**, 154
- Vasilevskis, S., Klemola, A., & Preston, G. 1958, [AJ](#), **63**, 387
- Walch, S., Girichidis, P., Naab, T., et al. 2015, [MNRAS](#), **454**, 238
- Winston, E., Megeath, S. T., Wolk, S. J., et al. 2007, [ApJ](#), **669**, 493
- Zavagno, A., André, P., Schuller, F., et al. 2020, [A&A](#), **638**, A7
- Zhang, Z.-B., Yang, E.-B., Choi, C.-S., & Chang, H.-Y. 2016, [MNRAS](#), **462**, 3243